

INTRODUCTION

In condensed matter systems, collective behavior of a lattice and its surroundings can lead to the manifestation of fascinating physical phenomena like quasiparticles. These excitations follow similar (but not identical) rules as their particle counterparts at different energy scales [4]. For example, the predicted energy of a magnetic monopole is estimated at about 10^{25} eV, whereas an emergent magnetic monopole exists in the 1 eV range [40]. As such, normally high-energy particles can be experimentally studied, albeit in a different form, at low energetic cost in lattice systems. The presence of such emergent phenomena are symptomatic of complex behavior; emergent monopoles can be found in the reciprocal space of ferromagnetic materials as a consequence of band topology and broken time-reversal symmetry. The intrinsic anomalous Hall effect arises from the presence of these magnetic monopoles [24], and can be measured in magnetotransport experiments.

$SrRuO_3$, a transition-metal oxide with itinerant ferromagnetism, hosts an anomalous Hall effect (AHE) [35]. It has moderate electrical conductivity, [54]. Highly conductive ferromagnets typically has a dominant extrinsic contribution to the AHE stemming from disorder, whereas moderately conductive ferromagnets like $SrRuO_3$, being labeled a 'bad metal', has a larger contribution from the intrinsic AHE [61].

Transition-metal oxides (TMOs) are a material class that exhibits rich and exotic behavior, due in no small part to their degrees of freedom being strongly interconnected; in $SrRuO_3$ alone, lattice strain affects magnetic and conducting properties [64], and the film thickness affects the magnetic moment [79] among other things. The reason underlying the behavior of TMOs lies in the transition metal atoms transferring their *s* electrons to the oxygen ions, leaving the strongly correlated *d* electrons to dictate transport and magnetic properties. Further, the effects experienced by the electrons like spin-orbit interaction, crystal field splitting and Coulomb repulsion are on the same energy scale, leading to a wide variety in behavior between TMOs, despite their similarity in structure and chemistry [13].

Creating layered epitaxial TMO structures opens a door to a new and still not fully explored range of physics. Interfacing $SrRuO_3$ with other transition-metal oxides was revealed to affect the shape of its AHE signal into unconventional shapes [44]. In recent years, the unusual behaviour of the anomalous Hall hysteresis loops of ultrathin $SrRuO_3$ films have raised a debate as to their origin. The topological Hall effect [73] [60] [62] [67] and coexisting uncoupled ferromagnetic domains [44] are postulated as possible explanations.

In this thesis, a tight-binding model for $SrRuO_3$ adapted from Ref.[44] is studied numerically and presented as an additional avenue for explanation of the exotic features of the AHE signal at $SrRuO_3$ interfaces. It posits that the low-energy band topology of $SrRuO_3$ can be used to explain the AHE signal at low temperatures, and is compared to low-temperature magnetotransport data of semiconducting $SrRuO_3$ in $SrTiO_3$ - $SrRuO_3$ - $LaAlO_3$ devices.

The structure of this thesis is as follows. In chapter 2, a literature review on the background information on the crystallographic, electronic and magnetic properties of $SrRuO_3$ is exposed, and an overview of the ordinary(OHE) and anomalous Hall effects (AHE), as well as a derivation of the quantal origin of the intrinsic AHE are given. Chapter 3 introduces the experimental techniques used for device synthesis and measurement. Chapter 4 reviews the methods used in obtaining and exploiting numerical models for $SrRuO_3$ monolayers, as well as $SrRuO_3$ - $SrTiO_3$ and $SrRuO_3$ - $SrIrO_3$ interfaces, with the results of the numerical analysis given in chapter 5. Experimental results are presented in chapter 6, and analysis is separated into quantitative and qualitative sections. In the qualitative section, the AHE signal is directly compared to the results of the numerical simulations. Concluding remarks and an outlook for future numerical models and transport experiments are given in Chapter 7.

2

NUMERICAL METHODS

2.1 NUMERICAL BERRY CURVATURE

2.1.1 *Creating a tight-binding system*

Experimental results can be compared to previously obtained results from articles and reports. Another type of comparison can be done using numerical simulation. Depending on the level of refinement, a model can provide either a general framework, a qualitative analysis or specific trends data can be expected to obey.

Since we know that the intrinsic AHE finds its origin in band-structure interactions, we need to model the dispersion relation of $SrRuO_3$. This could involve the creation of lattice points defined by a strong periodic potential [76] related by hopping values, generating trajectories in energy-momentum space that match the low-energy behavior of $SrRuO_3$. Such an approach is known as a tight-binding model.

A tight-binding approach is debatable in its relevance to $SrRuO_3$, as it is a one-electron model [4], and $SrRuO_3$ has moderate electron-electron interaction [70]. The transport properties of $SrRuO_3$ changing from metallic to insulating with decreasing film thickness is not simply ascribable to defect scattering, but is closely related to film stoichiometry and the degree of electron-electron correlation [78]. As such, despite the fact that it should have the largest response to the top gate due to a longer screening depth, capturing the qualitative physical response of the semiconducting $SrRuO_3$ sample could prove to be beyond the capabilities of a correlation-free model.

Using code from the Python library Kwant [45], a tight-binding model can be generated and passed to a solver in order to calculate physical properties of the system. The creation of a tight-binding system with Kwant is as follows. First, a mathematical graph (a set of nodes [2]) is created by calling an instance of `kwant.lattice`. The nodes are Bravais lattice sites that can be arranged with built-in libraries of `kwant.lattice` (eg. 'honeycomb', 'square', 'kagome') or any arbitrary shape using `kwant.lattice.general`. The tight-binding model is created through defining onsite energies on the nodes and connecting them by defining hoppings. Leads (tight-binding systems with translational symmetry in at least one direction) are attached to the system so that transport properties between leads can be probed by the Kwant solvers. Before it can be passed to solvers, the system is finalized, which sets the tight-binding graph but leaves the matrix elements open to change [45].

The numerical computation of the AHE requires knowing the periodic band structure of the lattice. In order to obtain periodic band structure information, we need a

periodic lattice. Since an edge presents a break in periodicity, that means the lattice should be infinite in the directions we want band structure information. A monolayer should be infinite in-plane (2D), and a thick structure should be infinite in 3D. The infinite system is then wrapped around, and the result is a k-space periodic system, with periodicity $2\pi/a$, a being the lattice constant (for a cubic system) [4].

2.1.2 Considerations on precision

The key to analyzing anomalous transport are the eigenvalues and eigenvectors. The solver `hamiltonian_submatrix` allows us to obtain the tight-binding Hamiltonian matrix, from which the eigenvalue and eigenvector sets can be extracted with the use of e.g. `scipy.linalg` functions.

Having obtained the eigenvalue and eigenvector set, we now need to implement Eq.?.?. Eq.?? implies that the Berry curvature is related to the Berry phase per unit area in parameter space. We note that Eq.?? relies on the existence of a function of a continuous set of eigenvectors and eigenvector derivatives, over which a contour integral is performed. Ideally, nothing would stop us from generating a continuous energy and eigenvector surface from our tight-binding Hamiltonian. We are however limited by computational restraints: a computer cannot be expected to yield an infinite set of values; such a set could not be stored in its memory. In any case, we only need a 'fine enough' [42] mesh, such that changes in the local Berry curvature are adequately visible. Finding a fine enough mesh can be done by comparing anomalous conductivity calculations to each other for increasing values of k-space precision, as a cut-off after which change is negligible can generally be found.

Globally, the integration of the Berry curvature over the whole ZBR should yield a quantized CN for an isolated energy surface, independent of the mesh value. However, the value of the CN may change with increasing precision [42]. By looking at the Fermi surface behavior of the model, we can estimate how fine our inquiry grid needs to be in order to capture energy surface changes on the order of linear behavior between adjacent grid points. Without this condition, nontrivial contributions may be washed out locally. The necessary grid spacing typically varies over the Fermi surface. An example of the importance of sufficient precision can be seen in Fig.1. In this case, a ZBR partition into a set of $50 * 50$ squares is sufficient to capture a majority of the information; higher resolution yields no visible change to the energy surface.

2.1.3 Calculating the Berry curvature

We may have resolved the problem of a discrete mesh, but we still need to express a continuous integral on a mesh. For a small enough k-space lattice spacing, we can consider adjacent points as directional derivatives relative to each other, i.e. $\partial k / \partial k_x$ is expressed as $k + b\hat{k}_x$, b the reciprocal space lattice spacing [80]. Calculating local

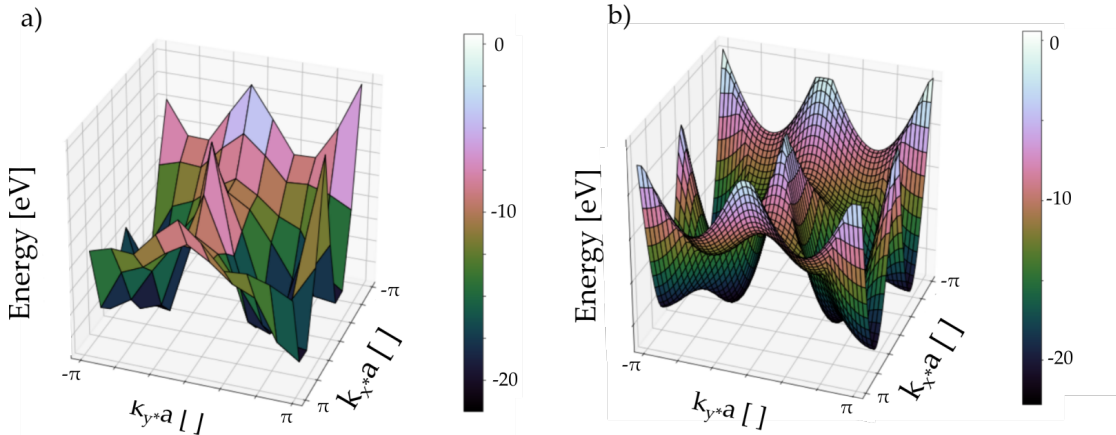


Figure 1: The lowest energy band surface of the SrRuO_3 - SrIrO_3 bilayer model that will be detailed in section 3.1, at $-\mu \cdot B = 0.25$ eV and a) $10 * 10$ b) $50 * 50$ ZBR partition.

Berry curvature is done by finding the anholonomy angle of a chain dot product of neighboring eigenvectors of the form [35]

$$\langle u_k | u_{k+b\hat{k}_x} \rangle \langle u_{k+b\hat{k}_x} | u_{k+b\hat{k}_x+b\hat{k}_y} \rangle \langle u_{k+b\hat{k}_x+b\hat{k}_y} | u_{k+b\hat{k}_y} \rangle \langle u_{k+b\hat{k}_y} | u_k \rangle \quad (1)$$

The neighboring eigenvectors are thus located on the corners of the smallest possible closed square loop in k-space. Eq.1 yields a complex number. We obtain the complex phase by taking its principal argument [8o]; this phase is none other than the Berry phase. The Berry phase over a unit contour is the integration of the Berry curvature over a unit k-space area [31], Eq.?? confirming this is dimensionally correct. Overall, this yields the following form for the sum of the Berry curvature from states below the Fermi level of band n:

$$K_n = \frac{1}{2\pi} \sum_{k, E(k) < E_F} \Im \ln \left(\langle u_{n,k} | u_{n,k+b\hat{k}_x} \rangle \langle u_{n,k+b\hat{k}_x} | u_{n,k+b\hat{k}_x+b\hat{k}_y} \rangle \langle u_{n,k+b\hat{k}_x+b\hat{k}_y} | u_{n,k+b\hat{k}_y} \rangle \langle u_{n,k+b\hat{k}_y} | u_{n,k} \rangle \right) \quad (2)$$

The anomalous conductivity (in units of the conductance quantum e^2/h) is then obtained by summing over all bands [8o].

The code used for obtaining the Berry curvature of our models can be found in Appendix 4.

2.1.4 Calculating the anomalous conductivity

Obtaining the Berry curvature over all of k-space is simply the addition of the Berry curvature results over every square in the ZBR. More interestingly for us will be the selection of contributions attributed to energies in a small window around the Fermi

level, since these will be the occupied states that contribute to the anomalous transport signal. This is the reason why a fine mesh is particularly important, so as to define the Fermi surface as precisely as possible. We know that at low temperatures and magnetizations, the domain of applicability of a tight-binding model, the Fermi level doesn't reside in a gap in $SrRuO_3$. It's possible that contributions neighboring the Fermi level, if not carefully excluded or included, would significantly affect the signal. Fig.2 illustrates this notion.

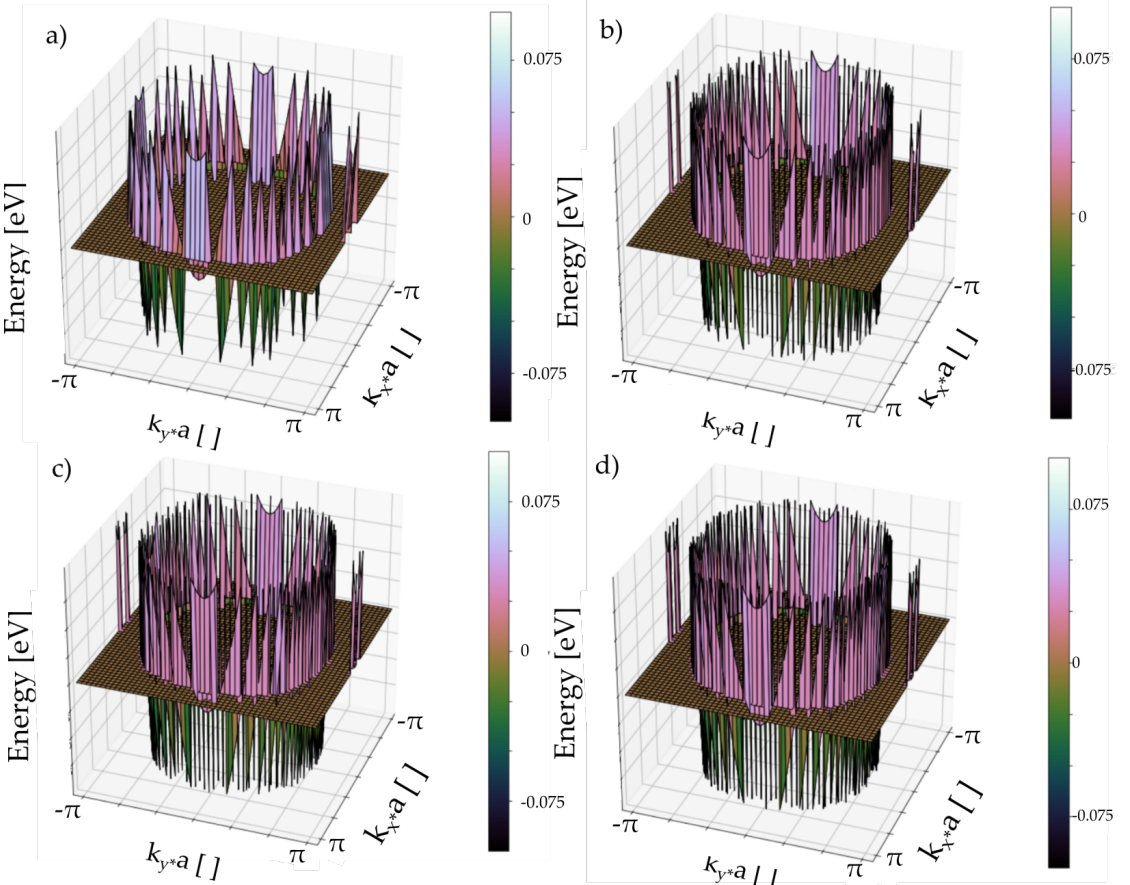


Figure 2: Sixth-lowest energy surface with states within 0.1 eV of the Fermi left intact and all others set to 0, for a) 50×50 b) 200×200 c) 300×300 d) 500×500 squares in the ZBR. We see that although the lack of significant difference between b) and c) might suggest sufficient precision; however, d) still indicates the inclusion of states that might have been excluded. Model used is the same as Fig.??.

Since the calculation of the Berry curvature is calculated with loops made of four states, it seems unjustified to include squares that have three of their four corners above the Fermi level, since those states in principle would not contribute to the signal. As such, it is safer to include squares whose four eigenvalues sum to an energy equal

to or smaller than the Fermi level. This will exclude certain states, but it will be a more accurate state selection. This can lead to a smoothing-out of point-like inclusions apparent particularly in Fig.2 b), c) and d). Further improvement of the code could include plaquette weighting factors (0 for plaquettes above the Fermi level, 1 below, and a number between 0 and 1 for squares cut by the Fermi level) as implemented in Ref.[38]. This method would also give a direct indication in the error of the numerical Berry curvature calculation [38].

3

NUMERICAL RESULTS

This chapter will exposit the tight-binding models that will be studied. For this, band structure analysis, local Berry curvature and anomalous conductivity will be calculated as a function of magnetic field splitting and relative Fermi level shift. The goal is to find a behavioral model for the low-energy anomalous Hall signal of the $SrRuO_3$ - $LaAlO_3$ films.

3.1 THE MODELS

The models we explore are based on tight-binding models elaborated in the supplementary information of Groenendijk et al. [44]. They include a monolayer of $SrRuO_3$, a $SrRuO_3$ - $SrIrO_3$ bilayer, and a $SrRuO_3$ - $SrTiO_3$ bilayer. Their tight-binding parameters were obtained via DFT LSDA+U calculations as described in Ref.[44].

3.1.1 Form of the models

All three models are based on the Ru , Ir and Ti t_{2g} orbitals d_{xy} , d_{xz} and d_{yz} . The $SrRuO_3$ monolayer tight-binding Hamiltonian basis is composed of the Ru t_{2g} orbitals in both z-spin projections. The effective bilayer models are composed of diatomic unit cells, mimicking the interface of $SrRuO_3$ with either $SrIrO_3$ or $SrTiO_3$. The Hamiltonian orbital basis is thus of length 12.

Ref.[44] adds the effect of a magnetic field through the Stoner model, $E_{\uparrow,\downarrow} = \epsilon(k) \pm I \cdot \frac{N_\uparrow - N_\downarrow}{N}$, with $\epsilon(k)$ the spinless dispersion and I the Stoner parameter [75]. This term enters the Hamiltonian as an additive contribution to the onsite energy, and is spanned from 0 to 2 m_B/Ru [44].

Fig.3 compares the band structure of the bilayer models from the paper to the numerical results obtained with Kwant:

Some clear differences are apparent. The Kwant models included SOC values sourced from Ref [44] for $SrIrO_3$ and from external sources for $SrRuO_3$ [54] and $SrTiO_3$ [50]. No explicit mention is made of the SOC values used to generate the plots referred in Fig.3 a) and b), so the comparison on that front is limited. However, the SOC value for $SrTiO_3$ has little importance due to the bands being far above the Fermi level, and is generally considered very weak (0.02 eV) [83] [50].

Another point of difference is the location of the Fermi level. Ref. [44] states that the Fermi level is set to zero, with no inclusion of this fact apparent in their tight-binding onsite parameters. The energy shift between the $SrIrO_3$ - $SrRuO_3$ models is

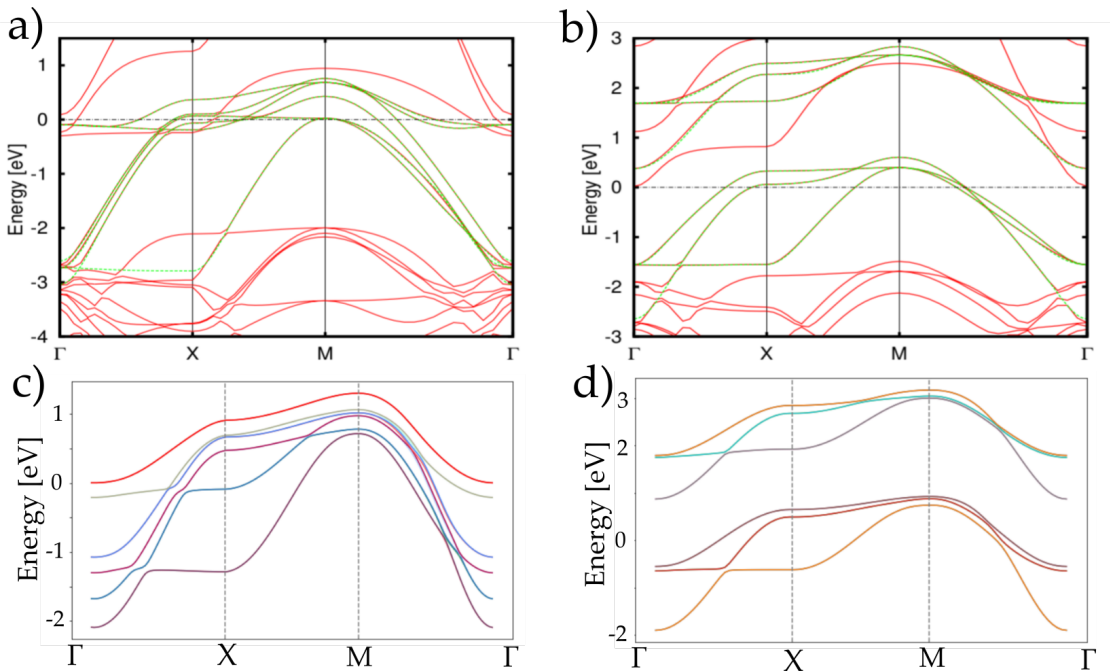


Figure 3: Numerical simulations of tight-binding bands for the bilayer models. From the paper, a) $SrIrO_3$ - $SrRuO_3$ and b) $SrTiO_3$ - $SrRuO_3$ in green [44], and calculated with Kwant c) $SrIrO_3$ - $SrRuO_3$ and d) $SrTiO_3$ - $SrRuO_3$. The models are presented in the nonmagnetic phase (spin-up and spin-down bands have no energy split).

approximately 0.5 eV. This means that this shift should be included in conductivity calculations to obtain the same results as the paper.

3.1.2 $SrRuO_3$ monolayer

Calculations of the Berry curvature of a 3D $SrRuO_3$ structure were performed in 2003 by Fang et al. [40], yielding the following result at $k_z = 0$ (Fig.??). Groenendijk et al. present numerical results under the form of band-structures, conductivity calculations and spin-polarizations. Explicit figures of Berry curvature calculations are limited to the negative-parity spin-orbit-parity-symmetric $SrRuO_3$ Hamiltonian. They show how dimensionality has affected the Berry curvature in Fig.4.

Despite the Berry curvature of the t_{2g} bands being displayed separately, we can still compare the Γ point value between Fig.?? and Fig.4: clearly, the near-degeneracy at low k is lifted and the bulk of the Berry curvature signal is shifted elsewhere in k -space.

The same bands are imaged numerically as a point of comparison in Fig.5.

We note a difference in the first two energy levels: an extra and opposite feature appears around $k = (0, 0)$. This is due to the way Scipy manages and sorts eigenvalues and eigenvectors. Eigenvalues are sorted in ascending order, which results in the

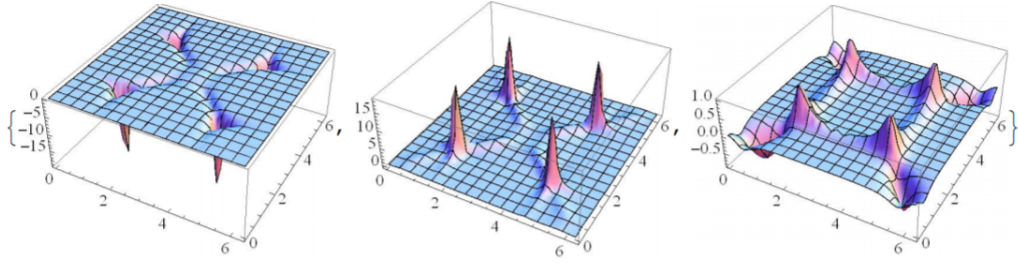


Figure 4: Berry curvature of the three negative spin-orbit-parity-projected t_{2g} bands of monolayer SrRuO_3 , ordered by increasing energy [44].

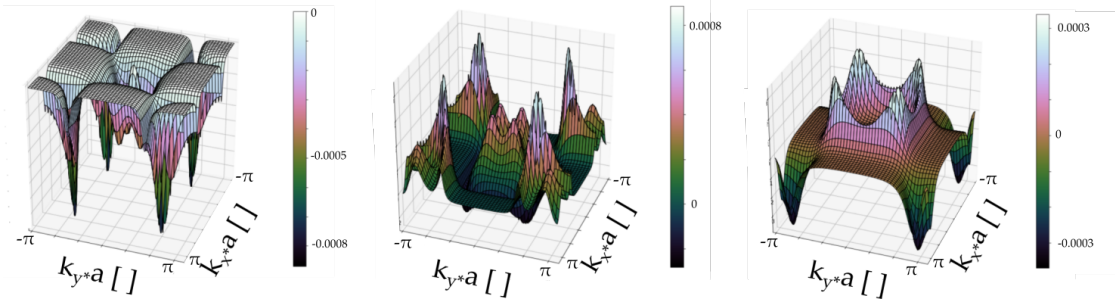


Figure 5: Berry curvature of the three negative spin-orbit-parity-projected t_{2g} bands of monolayer SrRuO_3 , ordered by increasing energy; Kwant numerical simulation. Note that the axes are different from the paper simulation.

energy band losing its connection to the orbital states. This is exemplified by switching the SOC on and off, as pictured in Fig.6. In Fig.6 a) and b) we see the eigenvalues are

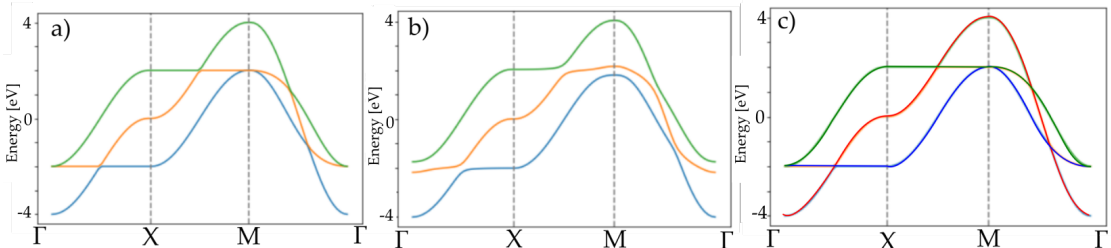


Figure 6: Dispersion of the three negative spin-orbit-parity-projected t_{2g} bands of monolayer SrRuO_3 . For a), b) colors exemplify bands as separated by Scipy; for c) colors identify bands from the orbital basis. SOC is switched on only for b).

sorted into bands from lowest to highest at all point in k -space. However, c) shows the actual repartition of eigenvalues according to orbital contributions. What this means is that if the onsite term as well as the hopping to and from an orbital were removed, it would remove one of the orbital bands in c) as opposed to one of the bands in a).

Comparing a) and c), we see that the top and bottom Scipy bands have the character of two of the orbitals, and the middle Scipy band is a combination of all three. As such, we cannot compare Fig.4 to Fig.5 directly without taking this into account.

The Scipy bands can still be used in calculations, as the goal of the simulations is to calculate the AHE conductivity. This is done by including states below the Fermi level, completely independently of what orbital they originated from. As such, we can use Scipy's bands but have to keep in mind that they do not retain the entire physical significance of the model when considered individually.

The $SrRuO_3$ model will be an integral part of our analysis, since the thin $SrRuO_3$ film will be the experimental focus. The surrounding materials in the devices, such as the $SrTiO_3$ substrate and the $LaAlO_3$ capping layer have the capacity to affect the $SrRuO_3$ dispersion at their interfaces, and as such are also interesting to model.

3.1.3 $SrTiO_3$ - $SrRuO_3$ bilayer

Modeling a bilayer in principle requires the addition of the third dimension, making Berry curvature analysis k_z -dependent. $SrTiO_3$ bands are located above the Fermi level of $SrRuO_3$, and thus are expected to not contribute to transport in any significant way. However, the Berry curvatures one obtains show changes from the $SrRuO_3$ monolayer, as exemplified in Fig.7. Comparing the Berry curvatures for the $SrRuO_3$ monolayer

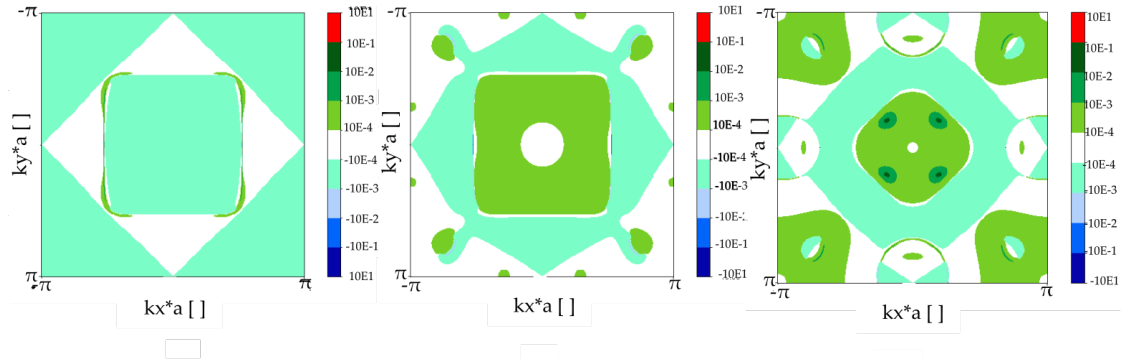


Figure 7: Berry curvatures for the three lowest energy levels of the simulated $SrTiO_3$ - $SrRuO_3$ bilayer at 0.5 eV spin splitting. A norm is used for clarity. ZBR partition is 400 * 400.

and the $SrRuO_3$ - $SrTiO_3$ bilayer reveal that the $SrTiO_3$ does have an important effect on the Berry curvature. Its full relevance to our study arises precisely from the fact that its bands do not contribute to the AHE signal. Since $LaAlO_3$ bands are also above the $SrRuO_3$ Fermi level, this $SrTiO_3$ model can provide some insight into the $LaAlO_3$ - $SrRuO_3$ interface in addition to the $SrTiO_3$ - $SrRuO_3$ interface.

3.1.4 $SrIrO_3$ - $SrRuO_3$ bilayer

Groenendijk et al. [44] study a double-loop scenario in the AHE signal, as pictured below:

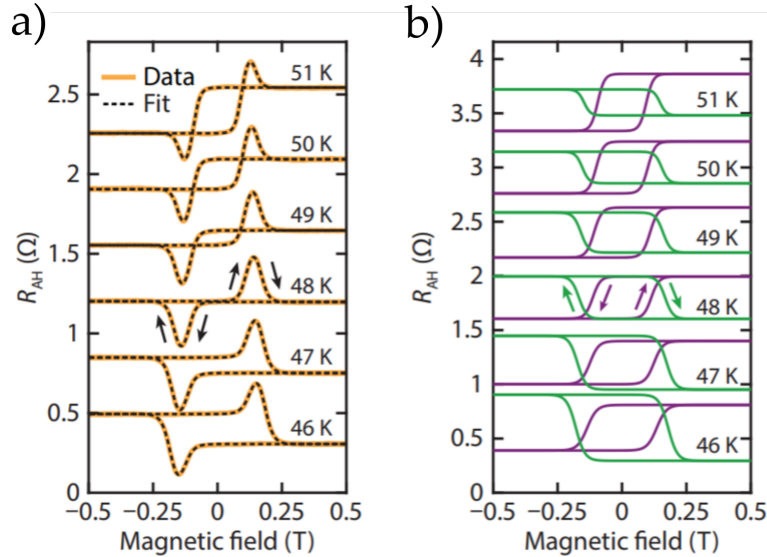


Figure 8: $SrTiO_3$ (substrate)/ $SrRuO_3$ (4 u.c.)/ $SrIrO_3$ (4 u.c.) data decomposition into double loops. a) The OHE-subtracted AHE data with double loop fit b) Double loop simulations of two anomalous Hall channels [44].

In their paper, they theorize the presence of two AHE channels of opposing sign that would explain the signal shape apparent in Fig.8 a). Others have attributed this to the topological Hall effect (THE), associated to topologically non-trivial spin textures such as skyrmions [67] [60]. However, sample-to-magnetic-field angle-dependent measurements [84] would provide evidence against the skyrmion explanation. Although the double-channel picture is a phenomenological rather than quantitative model, it provides credible qualitative reasoning for the shape of the AHE signal.

The focal point of their analysis is the comparison of the positive AHE contribution from a $SrIrO_3$ - $SrRuO_3$ - $SrIrO_3$ sample from 35 K to 58 K to the negative AHE contribution of the $SrTiO_3$ - $SrRuO_3$ - $SrTiO_3$ sample at the same energy range [44]. This would imply that the double-loop phenomenon is purely interface-driven. Thus, although it will not be included in our comparison to experimental data here, the $SrIrO_3$ - $SrRuO_3$ interface provides an interesting playground for exploring the AHE conductivity in $SrRuO_3$.

3.2 MODEL PARAMETERS

The parameters for obtaining experimental data include the Fermi level shift, the magnetic field and the temperature. The Fermi level shift can be included in our measurements as the inclusion of states below a value different from 0 (the Fermi level is set to 0). The magnetic field phase is not a geometric phase, and thus does not need to be included in the tight-binding model directly. Instead, magnetic field and temperature manifest in the magnetization function $M(B, T)$. For the thermal magnetization, we use the same function as in Ref.[44], the Stoner model for itinerant ferromagnets:

$$M_1(T) = M_0 \left[1 - \left(\frac{T}{T_C} \right)^2 \right]^{\frac{1}{2}} \quad (3)$$

A Heaviside-type function can be used for the magnetic-field-dependent portion of the magnetization. However, a better alternative might be a non-infinite slope at the transition point. This can be done with two offset Langevin or Brillouin functions, or a set of two hyperbolic tangent functions. The temperature dependence of the magnetic coercivity $B_c(T)$ is also included as a linear function.

$$\begin{cases} M_{2,down}(B, T) = M_1(T) * [\tanh(B * slope - B_c(T))] \\ M_{2,up}(B, T) = M_1(T) * [\tanh(B * slope + B_c(T))] \end{cases} \quad (4)$$

This leaves us with a relatively complete magnetization function.

Data collection is done by first generating the eigenvalue and eigenvector set for each value of magnetization. The states can then be dynamically selected by choosing the threshold that each k-space square must sum to. In this way, a colormap of the conductivity value can be made, as pictured in Fig.9. From this, it is straightforward to image the conductivity variation for any path through parameter space.

3.2.1 $SrRuO_3$ monolayer

Band structure and monopoles

The band structure of the $SrRuO_3$ monolayer can be seen in Fig.10. In view of the discussion of the intrinsic AHE originating from avoided band crossings, we can locate where these crossings take place in k-space. Recalling the way Scipy sorts eigenvalues, we know that the bands in Fig.10 do not have a 1-to-1 correspondence to the possible states of an electron in a single orbital, but are combinations of these bands. Turning the SOC on and off, this time including spin splitting, should give us a good idea of where the orbital bands have avoided crossings. We only expect these interaction between the SOC-coupled bands, given by the following relation:

$$\lambda \cdot [\sigma_x \otimes L_x + \sigma_y \otimes L_y + \sigma_z \otimes L_z] \quad (5)$$

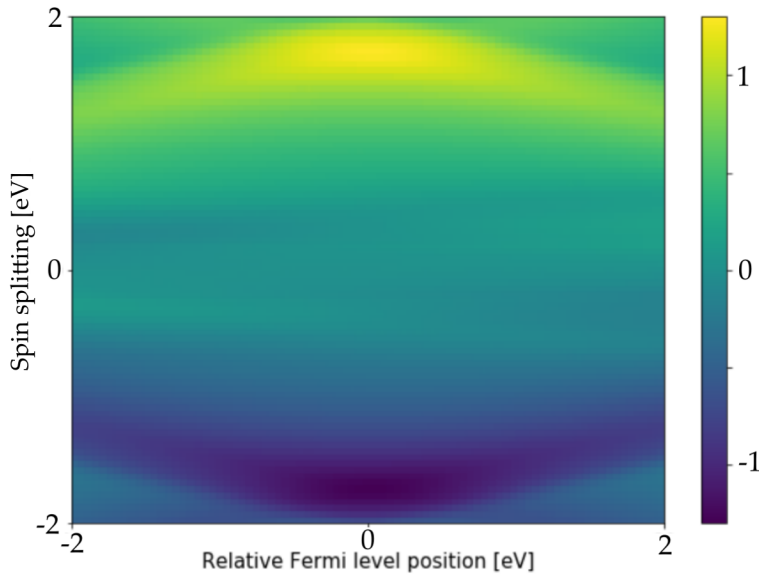


Figure 9: Colormap of conductivity in spin splitting - Fermi level parameter space for the $SrRuO_3$ monolayer model.

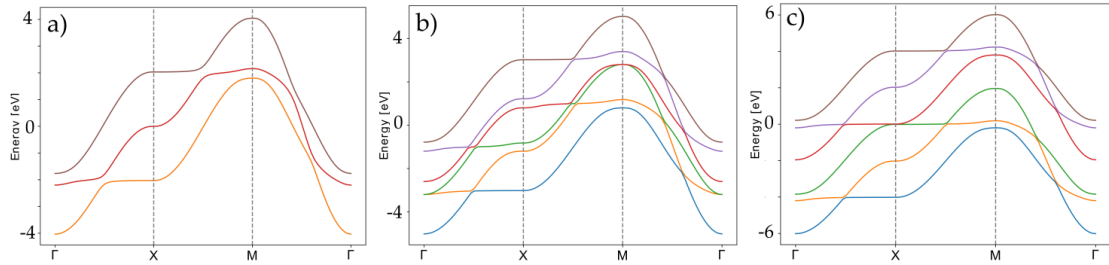


Figure 10: $SrRuO_3$ ML band structure for spin splitting of a) 0 eV, b) 1 eV and c) 2 eV.

with λ is half the strength of the SOC [18], \otimes the Kronecker product, $\sigma_{x,y,z}$ the Pauli matrices and $L_{x,y,z}$ the orbital momentum operators. In orbital basis, the matrix form of the SOC is:

$$\begin{aligned}
 & |\uparrow, yz\rangle \begin{pmatrix} 0 & -i\lambda & 0 & 0 & 0 & \lambda \\ i\lambda & 0 & 0 & 0 & 0 & -i\lambda \\ 0 & 0 & 0 & -\lambda & i\lambda & 0 \\ 0 & 0 & -\lambda & 0 & i\lambda & 0 \\ 0 & 0 & -i\lambda & -i\lambda & 0 & 0 \\ \lambda & i\lambda & 0 & 0 & 0 & 0 \end{pmatrix} \\
 & (6)
 \end{aligned}$$

(7)

where \uparrow , \downarrow correspond to the electron spin state and xy , xz , yz are the $SrRuO_3$ t_{2g} orbitals. The sets of SOC-coupled orbitals are thus $(|\uparrow, yz\rangle, |\uparrow, xz\rangle, |\downarrow, xy\rangle)$ and $(|\downarrow, yz\rangle, |\downarrow, xz\rangle, |\uparrow, xy\rangle)$. This means that we can expect both trivial (intragroup) and non-trivial (intergroup) crossings.

At no spin splitting, orbital bands for both spin values are perfectly superposed. Since there is no SOC between these bands, there can be no avoided crossings. With increasing spin splitting magnitude, the *down*-type bands will split away from the *up*-type. Since $SrRuO_3$ is a majority down-spin ferromagnet, down spins see a reduction in energy with increasing exchange coupling, while up spins have to pay an energy cost; Fig.10 shows this process. Avoided crossings will occur when two SOC-coupled bands start to cross. We exemplify this in Fig.11 by switching the SOC on and off for a spin splitting of 0.5 eV.

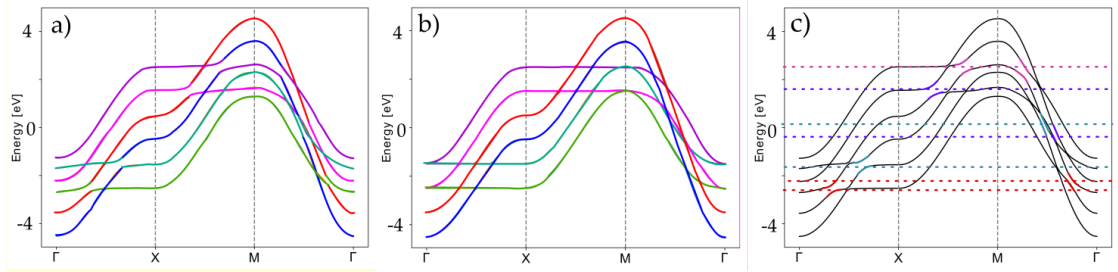


Figure 11: $SrRuO_3$ monolayer crossings along tetragonal high-symmetry trajectories. Color is used to visualize separate orbital character. a) with SOC b) without SOC c) locations of anti-crossing pairs; dotted lines of the same color indicate a pair of Weyl nodes of opposite chirality. The tetragonal high-symmetry points are illustrated in Appendix 5.1.

In Fig.11, we see the locations of anti-crossings along the main high-symmetry directions. Other crossings are likely to exist elsewhere in k -space. Fig.11 however can serve as a useful illustration of a key concept. We see that most anti-crossing pairs are not both located at the same energy level. This means that the occupation of one of these pairs will result in an anomalous velocity contribution that would not be erased by the simultaneous equal and opposite contribution that would come from occupying the pair.

Berry curvature

We can expand beyond the high-symmetry points to the entire ZBR, which repeats periodically in 2π . In the simulations, the lattice parameter is set to one. This means that the periodicity in k -space is reduced to $2\pi/a = 2\pi$ in both lattice directions. In this fashion, we can spot points of avoided degeneracy by the large Berry curvature localized in certain k -space points.

In this subsection, 'bands' refer to the Scipy lowest-to-highest sorted bands, and not the orbital-associated bands; this is because the calculation is done with the Scipy bands. As such, the analysis of Berry curvature is limited in its physical meaning when done band-by-band. It should, however, serve to reveal where points of large Berry curvature are.

An important question remains the necessary k-space partition precision required to calculate the Berry curvature. This question will be of particular importance in the next subsection, when the conductivity is calculated. The conductivity calculation relies on the precise inclusion of states below the Fermi level and on the integration on small enough loops that do not wash out important anholonomy angle contributions. The calculation of the Fermi level for each band only relies on the latter, and it is difficult to appraise beyond what visual means can tell us. As such, this subsection will comprise of a first look at the Berry curvature over all k-space with a partitioning of $300 * 300$. Additionally, it will be most informative to once again consider a spin splitting of $0.5eV$, since it will then be possible to compare anti-crossing locations with subsection 3.2.1.

The Berry curvature of the 6 bands associated to the 6 orbitals, using the code in Appendix 4, can be seen in Fig.12. From Fig.12 we can deduce that the avoided cross-

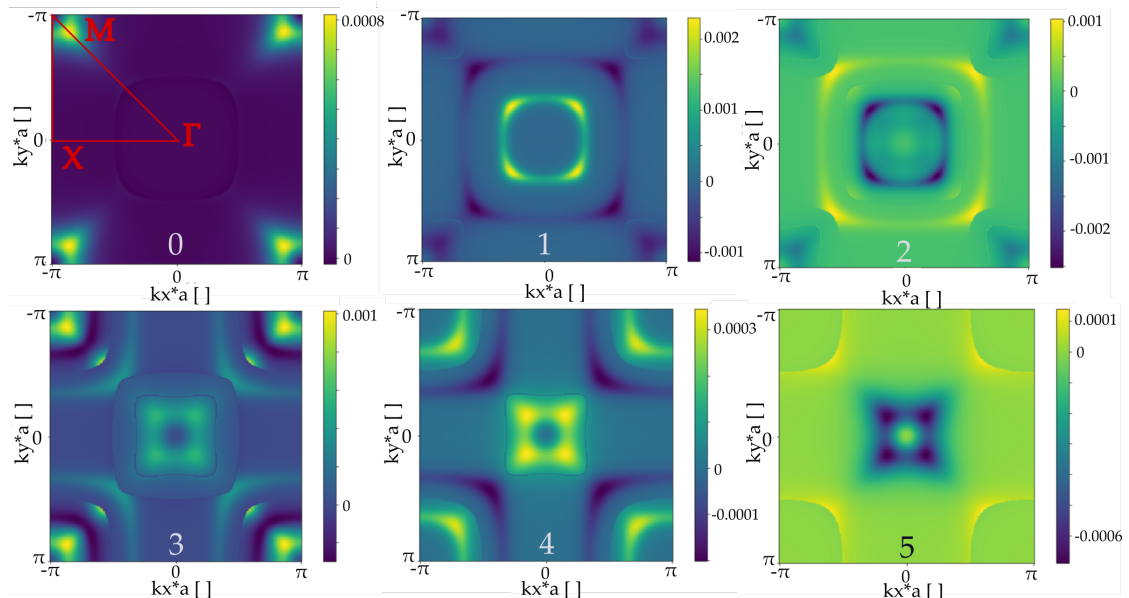


Figure 12: Berry curvature over the first ZBR for the six $SrRuO_3$ bands. Numbers indicate Scipy order. On the zeroth band, the tetragonal high-symmetry trajectories are indicated in red. k-space partitioning is $300 * 300$.

ings are located principally on the high-symmetry points. We thus know, using the information obtained in subsection 3.2.1, where the avoided crossings are.

From Fig.12 it appears that bands 0 and 1 share an additional avoided crossing at M , which was not accounted for in Fig.11. However, since the crossing pair is likely very close together near M , it is unlikely that their effects do not cancel simultaneously.

Fig.11 indicates that the avoided crossings most likely to be affected by the top gate experiment are the ones closest to $E = 0$, as their partners are separated in energy by 1 eV or more ('blue' and 'purple' crossings). Their position close to the Fermi level implies that a top gate, both positive and negative, could have an important effect on the Berry curvature signal.

The avoided crossings are prone to shifting in k-space and in energy with changing values of spin splitting. The conductivity calculation will reveal how the signal is affected.

Intrinsic anomalous conductivity

Only states occupied by electrons can manifest in transport. As such, studying the conductivity of an entire Scipy band by itself makes little sense, as the bands are not separated by a gap. Instead, the conductivity is calculated by the inclusion of all states below the Fermi level of all the bands together. Fig.13 presents a visual example.

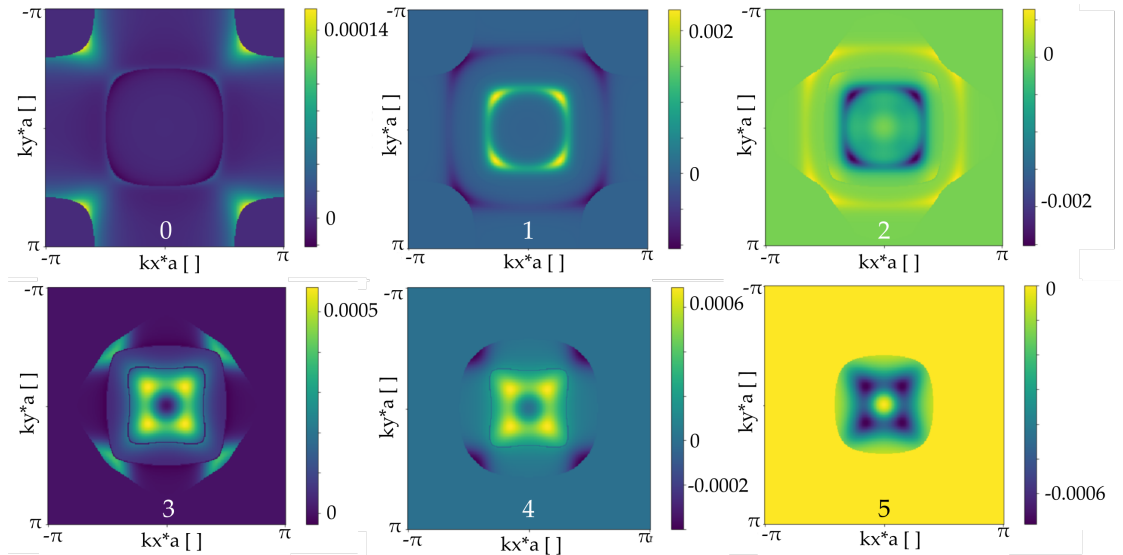


Figure 13: Berry curvature for states below $E = 0$. Numbers indicate Scipy order. k-space partitioning is $300 * 300$.

The partitioning of k-space has been limited to $300 * 300$. This is due to the appearance of a signal anomaly visible at higher precision; the details are in Appendix 5. Comparing Fig.13 and Fig.12, there is a clear signal exclusion that takes place. As such, as long as the pair anti-crossings are not occupied simultaneously, an AHE signal will be produced by the non-compensated anti-crossings.

Using the colorplot seen in Section 3.2, we can visualize how the changes in chemical potential and magnetization affect the AHE signal. A note should be made about the realistic Fermi level shifts that can be achieved. Shimizu et al. [69] conducted ion-gating experiments on $SrRuO_3$ thin films. The ionic liquid used had a capacitance of about $10^{-5} F cm^{-2}$. For a 5 u.c. $SrRuO_3$ film they predicted a carrier change of $\pm 2.5 * 10^{14} cm^{-2}$ for an applied gate voltage of $\pm 4V$, yielding a change of about $\pm 6\%$ in the longitudinal resistivity. Experimental results showed changes of $+2\%$ and -5.5% . The change in anomalous conductivity was much larger, reaching $\pm 40\%$ at 2 K [69]. The $SrRuO_3$ - $LaAlO_3$ films prepared for this report have a capacitance of $1.05 \cdot 10^{-11} F$. $\pm 4V$ results in an accumulation of charge of $\pm 2.6 * 10^8$ electrons on the surfaces of the dielectric. On the surface of the large Hall bar devices made for this experiment, this yields a charge carrier concentration of $6.5 * 10^{12} e/cm^2$, about two orders of magnitude less than Ref.[69]. Our experimental results will show a $\pm 2\%$ change in the anomalous conductivity for a 5 u.c. $SrRuO_3$ film at 10 K, and a $\pm 17\%$ change at 1.5 K (Fig.??). A $\pm 26\%$ is seen for the semiconducting $SrRuO_3$ film, showing that while the effect is reduced compared to ionic gating, the resulting change is of the same order for the semiconducting film with a solid gate, due to the larger field penetration depth. The density of states at the Fermi level would have to be considered in order to connect this to a Fermi level shift. As such, the link from model to experiment will have to be retroactive; considering a shift spread of $\pm 2 eV$, since that is the total energetic spread of the $SrRuO_3$ bands at 0.5 spin splitting (cf. Fig.10), and comparing the observed behavior to the model, it might be possible to glean the effect of the top gate in terms of a Fermi level shift. Fig.14 shows that changing the Fermi level has the power to reverse the sign of the AHE signal at low spin splitting magnitude (< 0.5). This effect arises for spin splittings of 0.5 eV and higher, and for relative Fermi level of -0.5 eV and lower. This Stoner splitting is within the correct magnitude for $SrRuO_3$ [30] [71] [39]. As such, we can realistically expect to manipulate the AHE sign of $SrRuO_3$.

Using the temperature- and magnetic field-dependent magnetization function as described in section 3.2, and associating each point to a conductivity value from the colormap, Fig.15 is obtained. Fig.15 is qualitative in that the time-dependent coercivity function $B_c(T)$ is taken as a relative coercivity, $1 - T/T_c$. As such, the values of the magnetic field are not important but are included as a general guide. The discreet jumps in the signal are due to the discreet nature of the signal values in the colormap.

The peak features are present for higher values of temperature, visible until about 80 K, or slightly more than halfway to the selected Curie temperature of 150 K, as visible in Appendix 5.3. However, we should only consider the tight-binding model as qualitative guidance for low temperatures. This argument merely lends some robustness to the signal: its features do not disappear at temperatures immediately higher than 0 K, meaning that it is not unrealistic to hope to observe similar features at low temperatures.

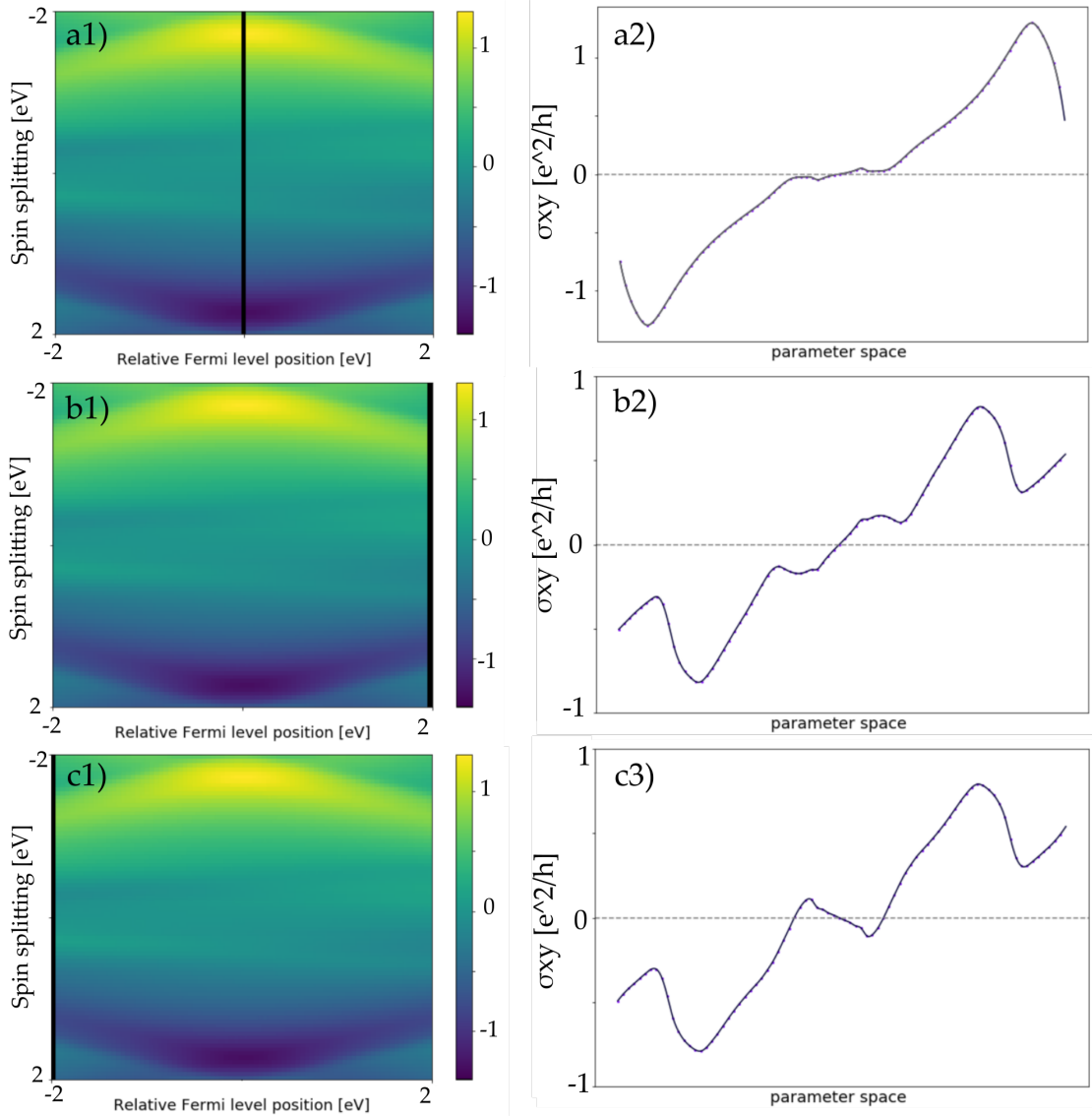


Figure 14: AHE signal as a function of spin splitting for fixed values of the chemical potential. Black lines on a1), b1), c1) indicate path taken in parameter space, and a2), b2), c2) show the AHE signal strength along the paths. k-space partitioning is $300 * 300$.

The features of the AHE signal change with the relative Fermi level, as expected from Fig.14. The signal is affected primarily in the following way at low temperatures, regardless of the sign of the shift: the saturation value of the signal is reduced, secondary peaks of opposing sign, and at low absolute values of magnetization there is a continuous evolution of magnetic switching. As expected from what was determined by Fig.14, we observe that the positive Fermi level shift induces no sign shift in the AHE signal at low magnetization amplitude, but rather two bumps. The nega-

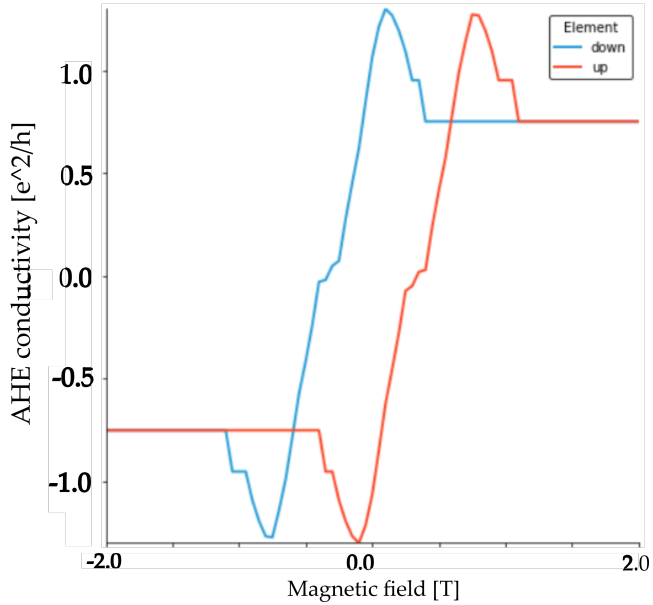


Figure 15: AHE conductivity signal of the $SrRuO_3$ monolayer model at 0 K and 0 eV relative Fermi level shift.

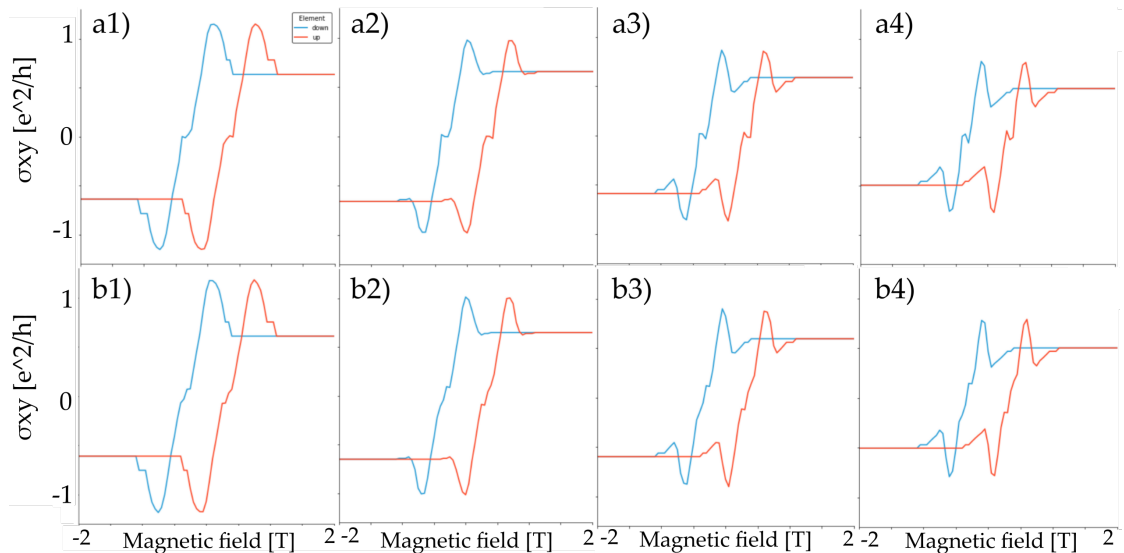


Figure 16: AHE conductivity signal of the $SrRuO_3$ monolayer model at 0 K. Relative Fermi level shift a1) 0.5 eV, a2) 1 eV, a3) 1.5 eV, a4) 2 eV, b1) -0.5 eV, b2) -1 eV, b3) -1.5 eV, b4) -2 eV.

tive Fermi level shift, where we expect to see the sign change, is increasingly visible with shift size. Fig.16 will be one of the qualitative bases with which we can approach measurements.

3.2.2 $SrRuO_3$ - $SrTiO_3$ bilayer

The $SrRuO_3$ - $SrTiO_3$ bilayer as described in [44] yields Fig.17. This model has 12 bands

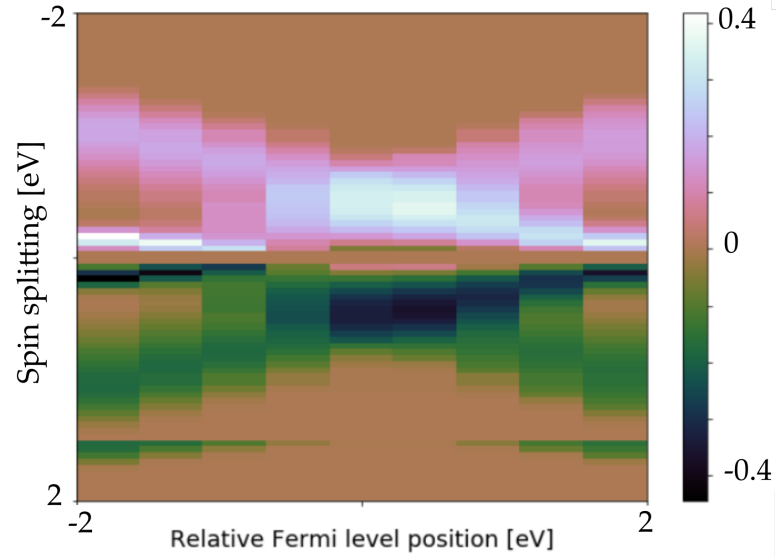


Figure 17: AHE of the $SrTiO_3$ - $SrRuO_3$ model from [44] as a function of spin splitting and Fermi level shift. k-space partitioning is $300 * 300$.

(the 6 $SrTiO_3$ t_{2g} bands are now included). The calculation was limited in Fermi level precision (9 points instead of 81 for each of the 81 magnetization points). The signal is zero at zero spin splitting for all values of Fermi level shift, as expected. We note the presence of a sign inversion close to the Fermi level for low values of magnetization. Fig.18 reveals several surprising things. A sign reversal at low energies takes place at 0.5 eV and -1 eV, so for both shift directions. Compared to the $SrRuO_3$ model, the sign reversal at 0.5 eV here is broader and closer to the Fermi level. Since both $LaAlO_3$ and $SrTiO_3$ are insulating interfaces with $SrRuO_3$, the $SrRuO_3$ - $SrTiO_3$ could model some behavior of the $SrRuO_3$ - $LaAlO_3$ samples, and these features should be taken into consideration. We note, however, that $LaAlO_3$ does not have t_{2g} bands, unlike $SrTiO_3$ and $SrRuO_3$.

This model does have some strong qualitative problems, however; the AHE signal drops to zero above a certain magnitude of spin splitting, which is not the expected behavior [44]. Looking at Fig.3, it is likely that monopole pairs group evenly above and below the Fermi level for a certain value of spin splitting. As such, the conductivity drops to zero.

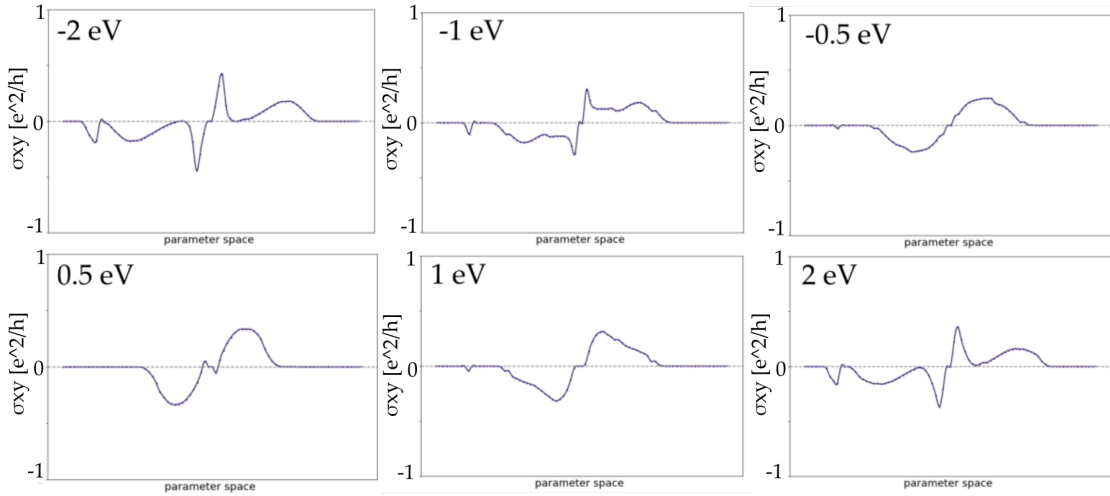


Figure 18: Magnetization sweeps of the AHE signal from Fig.17 at different values of energy shift from the Fermi level. Sweeps are done from -2 eV to 2 eV spin splitting.

3.2.3 $SrRuO_3$ - $SrIrO_3$ bilayer

Unlike $SrTiO_3$, $SrIrO_3$ has tight-binding bands that contribute at the Fermi level. Fig.3 a) shows how dense these states are at the Fermi level. Simulations of the AHE signal with varying k-space partitioning precision and spin splitting data points demonstrate the need for high precision. Fig.19 shows vast signal differences at low energies. Since we are interested in the Fermi level and its close vicinity, a high-resolution calculation was performed between -0.5 and 0.5 eV for the spin splitting, while keeping a 4 eV chemical potential sweep, for completeness. Of course, since $SrIrO_3$ is also metallic, a top gate on a $SrTiO_3$ - $SrRuO_3$ - $SrIrO_3$ sample would have a lower chance of affecting the $SrRuO_3$, as an electric field would be mostly screened before attaining it. However, there is the possibility of back-gating the sample, as shown in Ref.[62] to remarkable results, including the reversal of the AHE signal. Even though it will not be an experiment, the $SrRuO_3$ - $SrIrO_3$ model is still relevant to our numerical study of the AHE signal in $SrRuO_3$. Fig.20 shows that the precision may still be too low, due to the appearance of discontinuous peaks, perhaps similar in origin to the nonphysical peak seen for the $SrRuO_3$ model (cf. Appendix 5). Two signal crests of opposite sign are hosted in the model from -1.5 eV to 1.5 eV. Since the model excludes ferromagnetic ordering for the $SrIrO_3$ bands, the AHE signal is entirely attributable to the $SrRuO_3$ bands. As such, we should see similarities between the signals of the $SrRuO_3$ model and the $SrRuO_3$ - $SrIrO_3$ model.

Close to the Fermi level, we see a switch in the signal sign at low magnetization. This effect is more pronounced for positive Fermi level shifts, reappearing after 1.5 eV. For negative Fermi level shifts, the effect disappears at -0.5 eV before briefly reappearing.

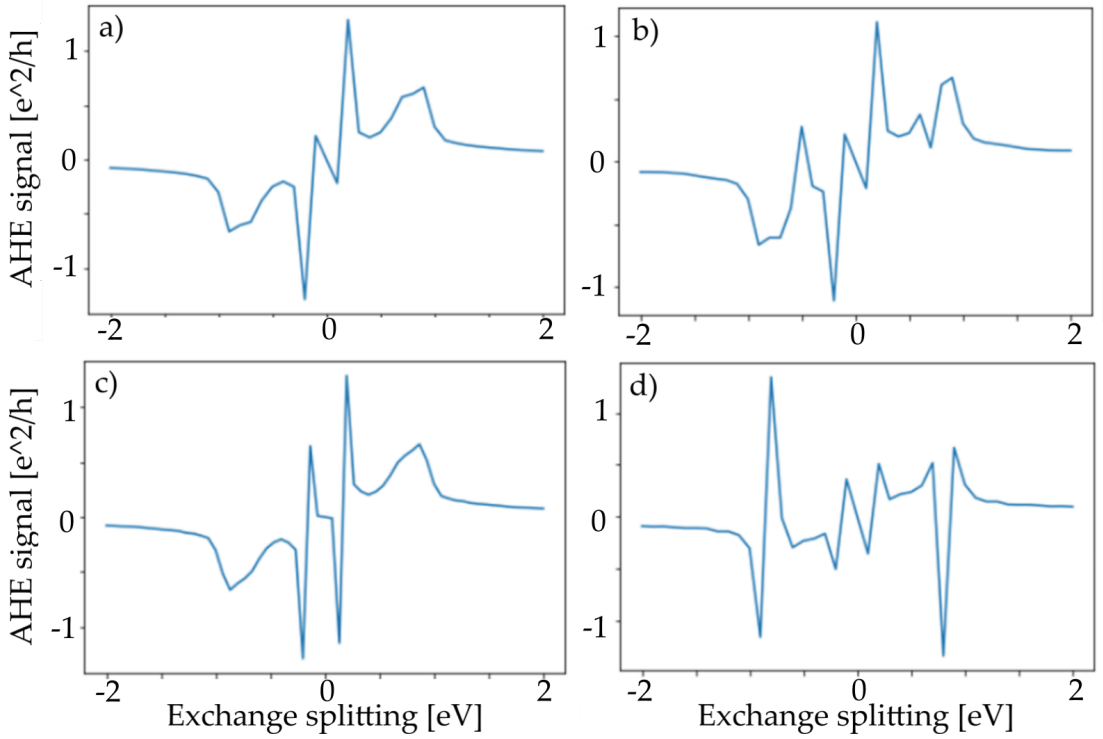


Figure 19: AHE of the $SrIrO_3$ - $SrRuO_3$ model from [44] as a function of spin splitting at the Fermi level. k-space partitioning is a), c) $300 * 300$, b) $200 * 200$, d) $100 * 100$ and number of data points is a),b),d) 41 and c) 61.

This complicated signal is no doubt onset by the strong SOC induced in the $SrRuO_3$ by the proximity with $SrIrO_3$, leading to complex interplay of bands not seen for lower values of SOC.

It would be interesting to attempt to modify the Fermi level of a $SrRuO_3$ - $SrIrO_3$ sample due to the rich low-energy reactions to the shift; however, the experimental reality would likely be quite different due to the small magnetization range over which the signal fluctuations occur, as exemplified below; the sign changes five times from -0.25 eV to 0.25 eV spin splitting close to the Fermi level, and evolves in a complex manner with Fermi level shift.

3.3 COMBINING CONTRIBUTIONS

In the two-loop model of Ref.[44], contributions are thought to arise from the two different interfaces of $SrRuO_3$ with other complex oxides. As such, we can combine the $SrRuO_3$ signal with the $SrRuO_3$ - $SrTiO_3$ model in order to see how the signal changes. Fig.22 reveals several interesting features. The case in which both contributions coexist at the Fermi level, originating from magnetization loops of the same shape, show

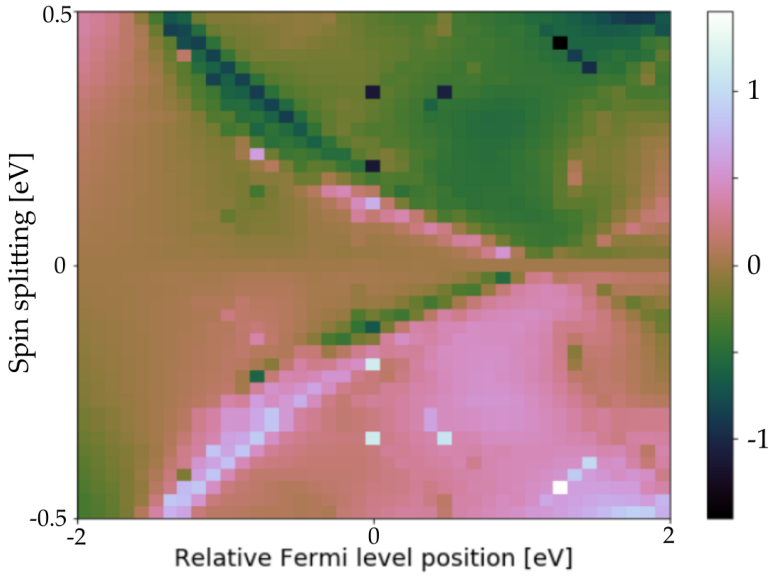


Figure 20: AHE of the $SrIrO_3$ - $SrRuO_3$ model from [44] as a function of spin splitting and chemical potential. k-space partitioning is $450 * 450$.

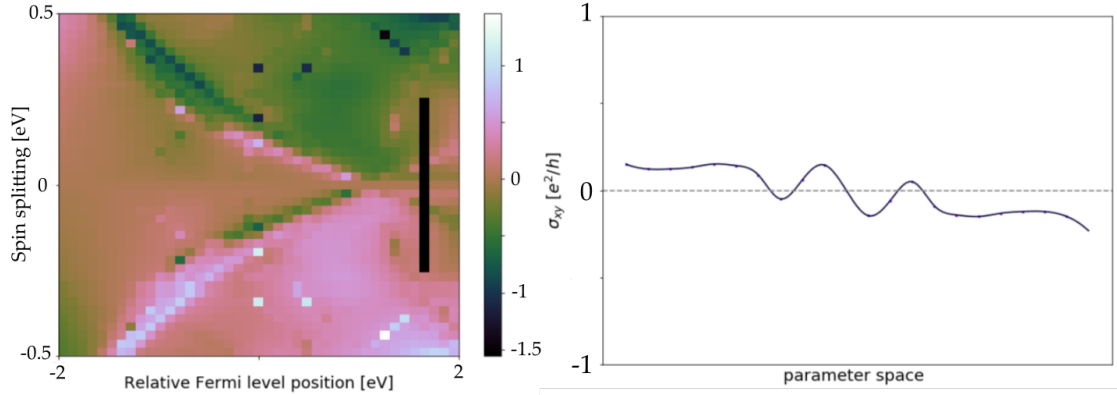


Figure 21: Magnetization sweep of the AHE signal at different values of energy shift from the Fermi level. Black line indicates path taken in parameter space.

little difference from the $SrRuO_3$ monolayer model in Fig.15. However, if the $SrRuO_3$ contribution experiences the effect of the top gate and the $SrRuO_3$ - $SrTiO_3$ contribution is unaffected, for example due to a penetration depth that doesn't span the depth of the film, low-magnetization behavior is suppressed. The clear switching signal close to zero magnetization of the accumulated $SrRuO_3$ model is sharply reduced by the presence of the unaffected $SrTiO_3$ - $SrRuO_3$ interface. Once this interface is affected, we see little difference between accumulation and depletion beyond a smaller separation

of the switching for accumulation. It is interesting to note that there are now two switches for accumulation as opposed to one for the $SrRuO_3$ model.

The influence of the $SrRuO_3$ - $SrTiO_3$ signal on the total AHE signal can be considered even at the Fermi level, as pictured in Fig.22 a) and b). If the magnetic domains differ, then the consequence for the final signal is even more pronounced than if two $SrRuO_3$ loops coexisted (cf. Appendix 5.9). Since there is no direct magnetic domain information that can be obtained via the transport experiments in this thesis, and since the model can be tuned by many different parameters, this type of manipulation should be done very carefully in order to avoid using unjustifiable parameter values in order to justify an observation. Nevertheless, this model could prove to be more valuable than the $SrRuO_3$ monolayer model, as it can yield information on both the participation of the $SrTiO_3$ - $SrRuO_3$ interface to the total signal, and on the degree of depletion and accumulation present in the sample at both interfaces.

The three models display similar low-energy features, and the higher field signal signs are mutually consistent. Whereas there is no guarantee the expected features will be visible at low temperatures and magnetizations in the $SrTiO_3$ - $SrRuO_3$ - $LaAlO_3$ samples, the $SrRuO_3$ model can serve as a general qualitative guide. The joint $SrRuO_3$ - $SrTiO_3$ and $SrRuO_3$ signal will also be considered on a secondary note, due to the delicacy required in using it appropriately.

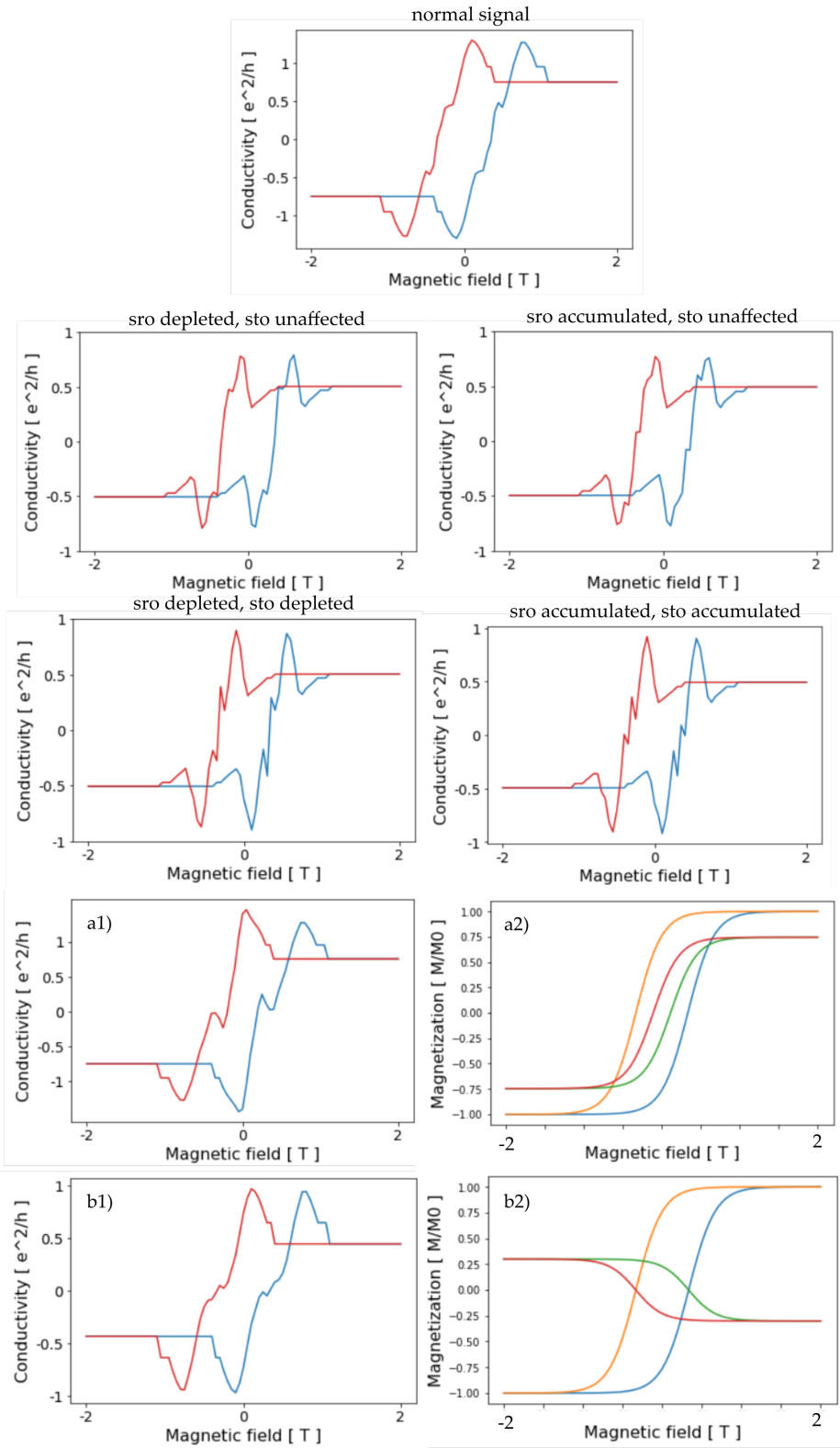


Figure 22: Numerical simulations of the superposition of the monolayer $SrRuO_3$ and $SrRuO_3$ - $SrTiO_3$ bilayer AHE signal for different depletion and accumulation scenarios. a1) Represents the signal arising at the Fermi level of both contributions from the magnetization loops in a2) where the $SrRuO_3$ monolayer signal is from the loop with larger coercivity. b1) Represents the same scenario except the $SrRuO_3$ - $SrTiO_3$ signal arises from a magnetization loop of opposite and reduced sign in b2). The $SrRuO_3$ and $SrRuO_3$ - $SrTiO_3$ contributions were considered to be of equal magnitude unless stated otherwise.

Part I
APPENDIX

APPENDIX A

4.1 APPENDIX A.1

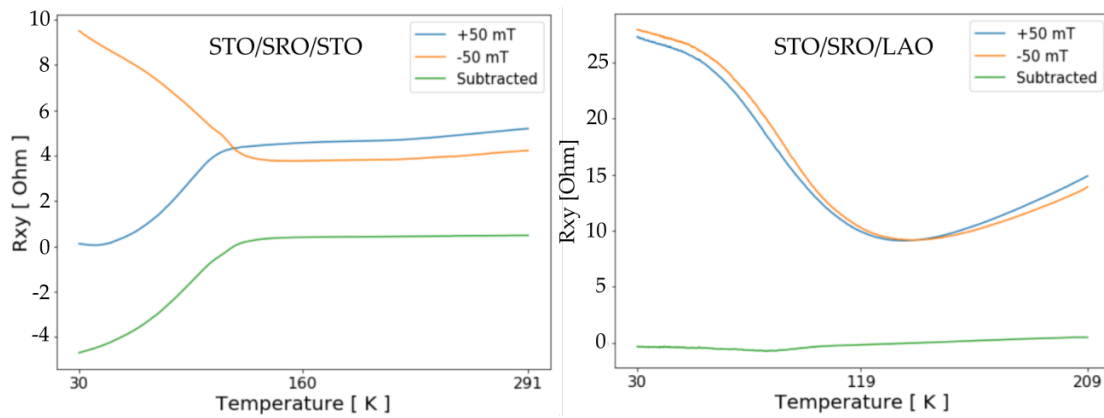


Figure 23: Field cooldowns for a STO/SRO(5 u.c.)/STO(10 u.c.) sample and a STO/SRO(4 u.c.)/LAO(10 u.c.) sample. The LaAlO_3 -capped sample shows higher resistance, possibly indicating a depleted layer in the SrRuO_3 . This makes SrTiO_3 - SrRuO_3 - LaAlO_3 samples more suited to top gate experiments. (We also note that the STO/SRO/LAO sample has 4 u.c. of SrRuO_3 , so perhaps the increase in resistance is dimensionally-driven.)

4.2 APPENDIX A.2

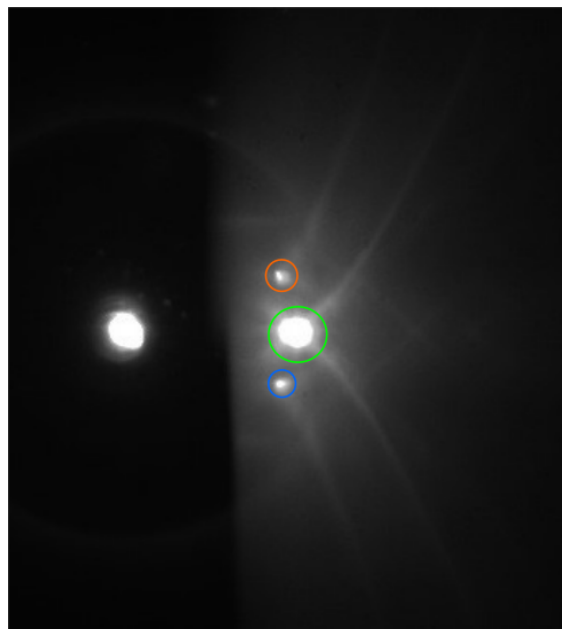


Figure 24: RHEED diffraction pattern. The spots are color coded according to their contribution in Fig.??

4.3 APPENDIX A.3

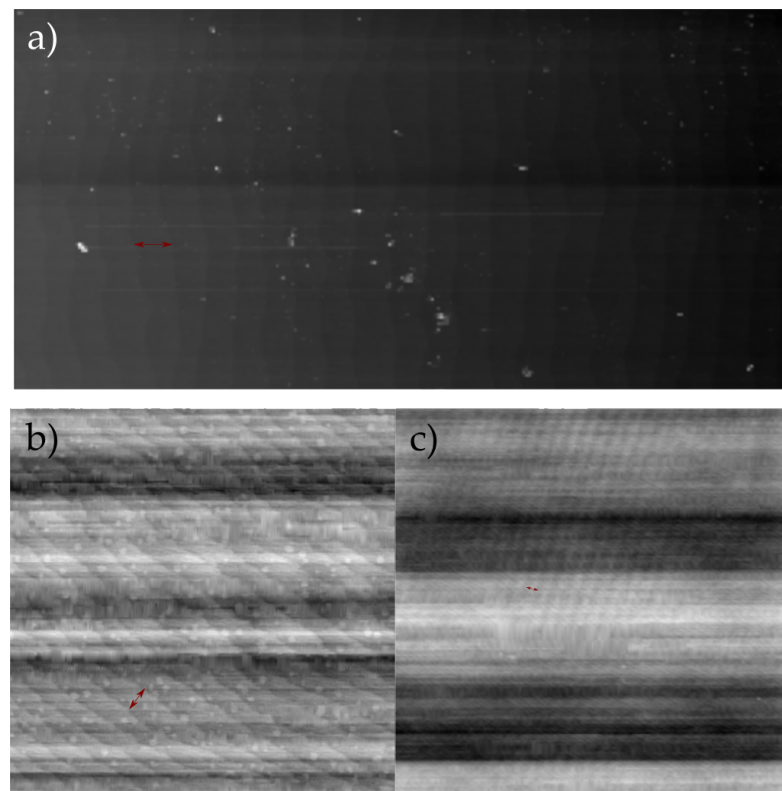


Figure 25: Atomic force microscopy (AFM) images of SRO₃₄, a sample grown in the same conditions as SRO₃₂. a) the $SrTiO_3$ substrate as received, b) a 5-by-5 and c) a 25-by-25 micron scan of the film surface. Red arrows indicate terrace width, showing the preservation of the step edges and the quality of the epitaxial growth.

4.4 APPENDIX A.4

Code used to obtain eigenvalues and eigenstates.

<https://github.com/helenespring/appendices>

4.5 APPENDIX A.5

Code used to determine a 2D map of coordinate points in k-space.

<https://github.com/helenespring/appendices>

4.6 APPENDIX A.6

Code used to obtain the Berry curvature and 2D plane contribution to the conductivity from the eigenvalues and eigenstates. It expects the externally generated coordinates and eigenvalue, eigenstate set using the previous two functions. <https://github.com/helenespring/appendices>

5

APPENDIX B

5.1 APPENDIX B.1

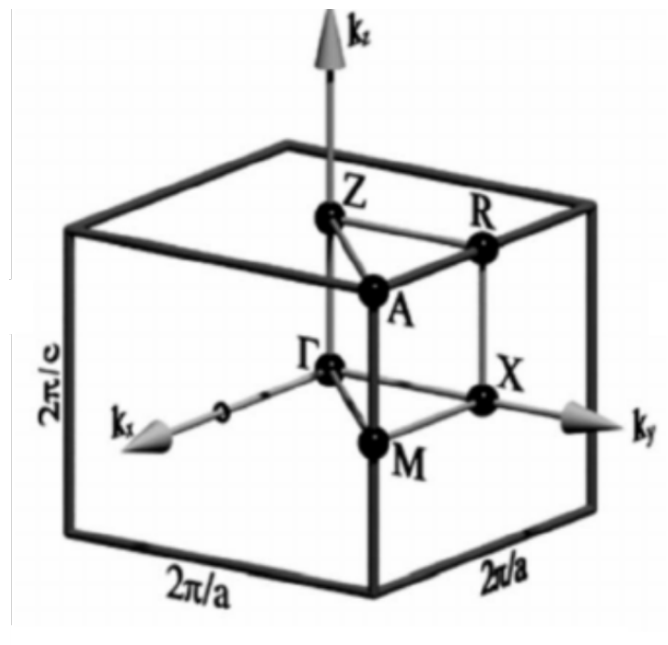


Figure 26: First Brillouin zone of a tetragonal lattice with high-symmetry points, from Ref.[43].

Since we consider a 2D model (x-y plane), Γ , X , M are the only high-symmetry points considered.

5.2 APPENDIX B.2

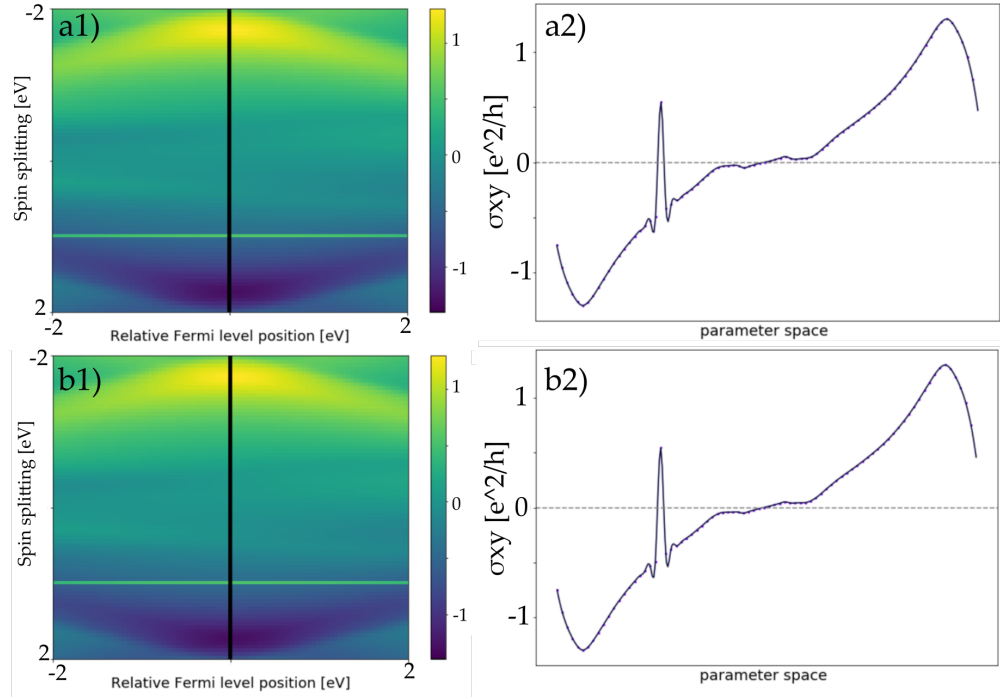


Figure 27: AHE signal as a function of exchange splitting for fixed values of the chemical potential. Black lines on a1), b1) indicate path taken in parameter space, and a2), b2) show the AHE signal strength along the paths. k-space partitioning is a) 350×350 and b) 500×500 .

At an exchange splitting value of -1, the signal suddenly changes sign for a single data point, so over a range of 50 meV. This anomaly is also present for all considered values of relative Fermi level position, from -2 to 2 eV. Values of the AHE signal around this point are listed in Table 1 at 0 eV relative Fermi level position: The contribution

Table 1: AHE anomaly as a function of exchange splitting and k-space partition

Exchange splitting [eV]	300×300	350×350	400×400	450×450	500×500
-1.1	-0.533	-0.532	-0.532	-0.533	-0.533
-1.05	-0.491	-0.491	-0.492	-0.492	-0.493
-1	-0.453	+0.546	+0.546	+0.545	+0.545
-0.95	-0.416	-0.417	-0.416	-0.417	-0.417
-0.9	-0.380	-0.380	-0.381	-0.382	-0.382

must arise from parts of the band structure either below -2 eV or above 2 eV, or both. As it turns out, looking at the band structure for -1.05, -1, and -0.96 eV of exchange splitting yield the origin of this signal: From Fig.28 we see that bands become degenerate at Γ and at M . This degeneracy is symmetrically lifted around -1 eV exchange splitting. At this crossing, massive contributions arise for the single-square Γ and M positions, 10^4 times larger than contributions per square on average in surrounding bands. These degeneracies are between SOC-coupled bands; in essence, the two anti-crossings roll into one point. As mentioned previously in passing, this should result in the presence of a Dirac cone. However, since it's far below the Fermi level, this should not result in a change of signal. At the degeneracy point, the signal jumps by $1.037e^2/h$ or $1.038e^2/h$. The signal then jumps by $-0.963e^2/h$ or $-0.962e^2/h$. The linear regression between the surrounding points has a slope of 0.755, leading to a difference of about $0.04e^2/h$. Taking this into account, the jump in signal is a quantized jump of $1 e^2/h$.

This means there is a problem with the numerical calculation. It is most likely due to the two Weyl nodes meeting on corners of a single integration square yielding a quantized signal. The same thing happens at the M point, but since it is above the Fermi level its signal is not registered by the conductivity calculation.

As such, the 300×300 partition, which washes out this signal, will be most qualitatively relevant to the experiments.

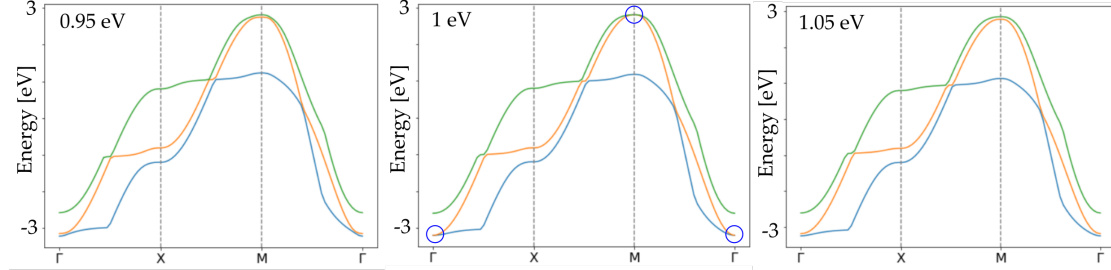


Figure 28: Scipy bands 1, 2 and 3. Blue circles indicate degenerate crossings.

5.3 APPENDIX B.3

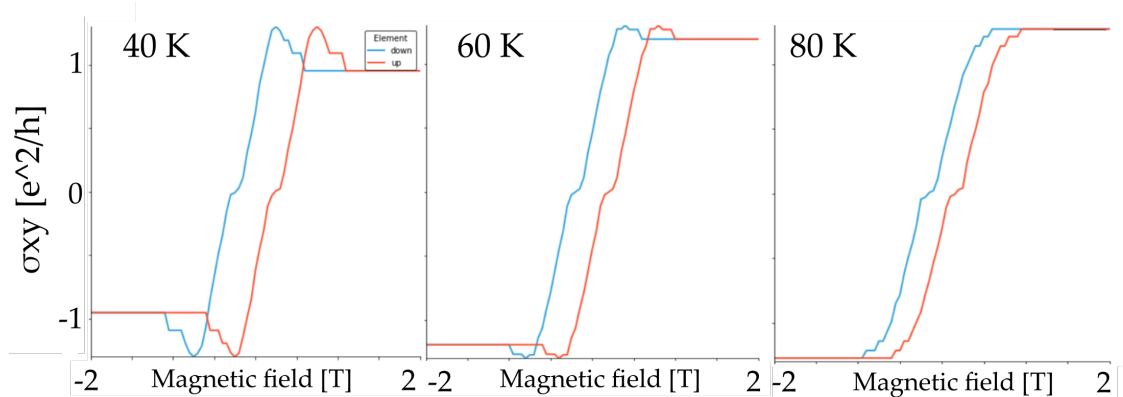


Figure 29: Change of AHE signal with temperature of the $SrRuO_3$ monolayer model.

5.4 APPENDIX B.4

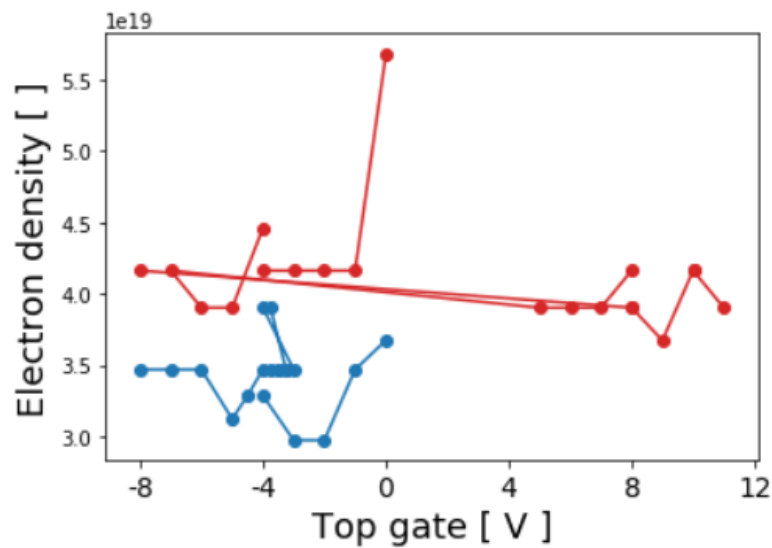


Figure 30: SRO13. Electron density at 1.5 K (blue) and 10 K (red) as a function of top gate voltage.

5.5 APPENDIX B.5

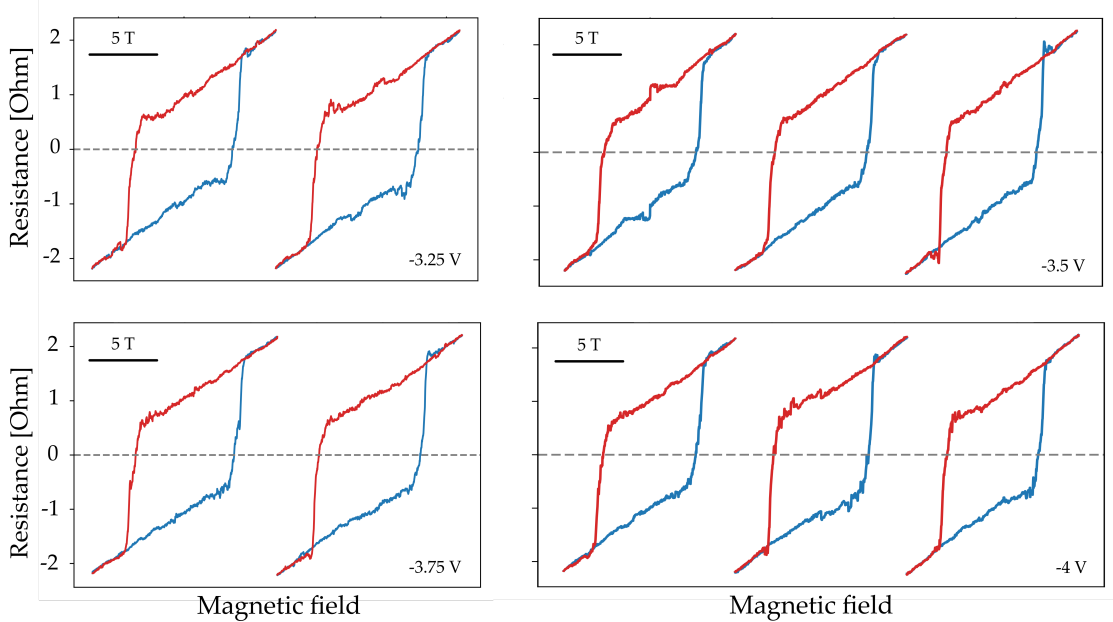


Figure 31: SRO13. Magnetic field sweeps at 1.5 K. With repeated measurements, the same loops are not obtained, and spurious features appear.

5.6 APPENDIX B.6

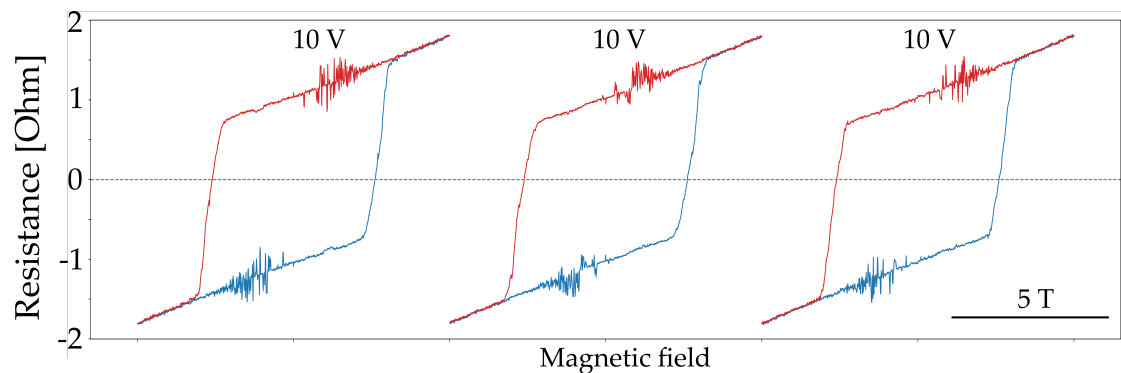


Figure 32: SRO₁₃. Antisymmetrized AHE conductivity at 10 K.

5.7 APPENDIX B.7

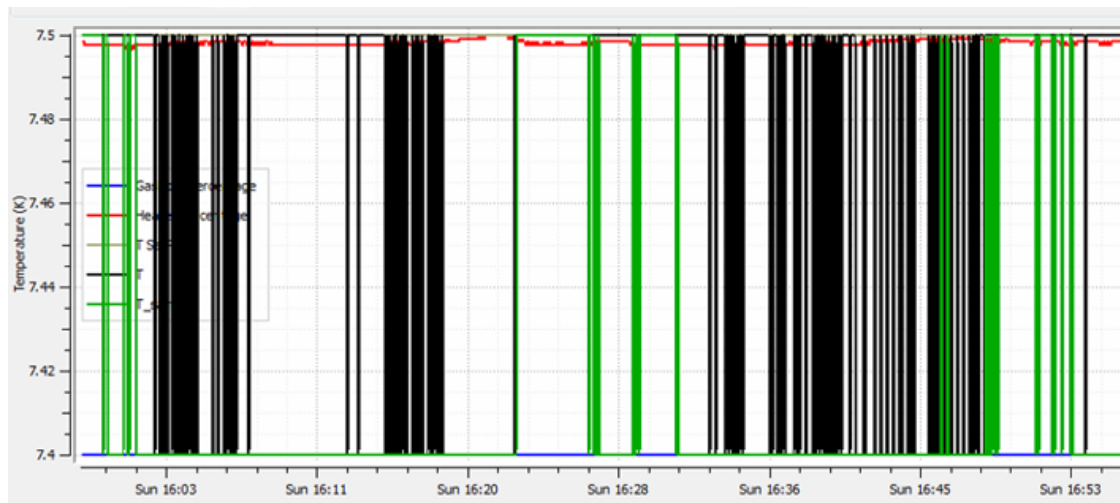


Figure 33: SRO32. Temperature drift as a function of time during a measurement at 7.5 K. The results are increasingly sensitive to changes in temperature at low temperatures, and as such this is a significant source of noise at low temperatures.

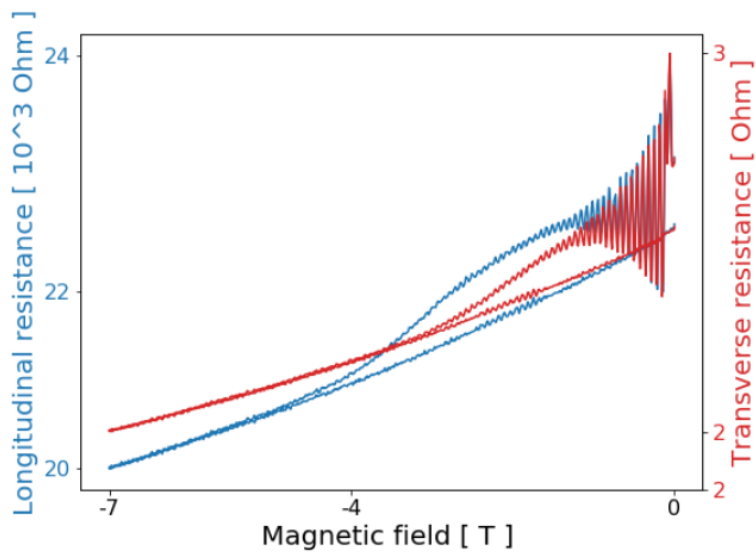


Figure 34: SRO₃₂. Presweep at 5 K shows signal fluctuations due to temperature drift.

5.8 APPENDIX B.8

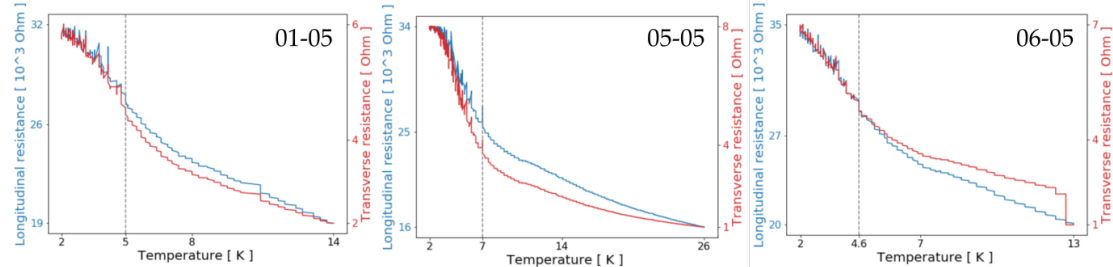


Figure 35: SRO₃₂. Cooldowns on different days show a changing boundary for the limit of the measurement module sensitivity.

5.9 APPENDIX B.9

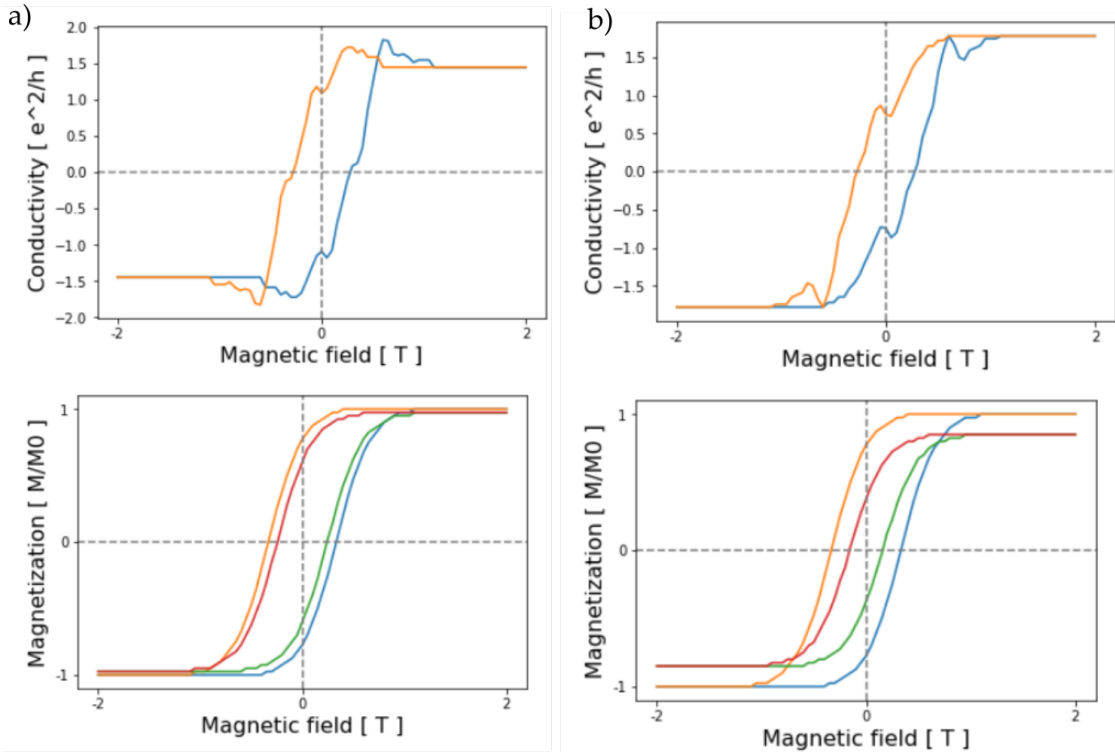


Figure 36: Two-loop signal for the $SrRuO_3$ model. a) the loop with smaller coercivity has a negative Fermi shift and b) positive Fermi shift. Since the parameter space is large (initial magnetization, coercivity, chemical potential), a large number of combinations exist.

5.10 APPENDIX B.10

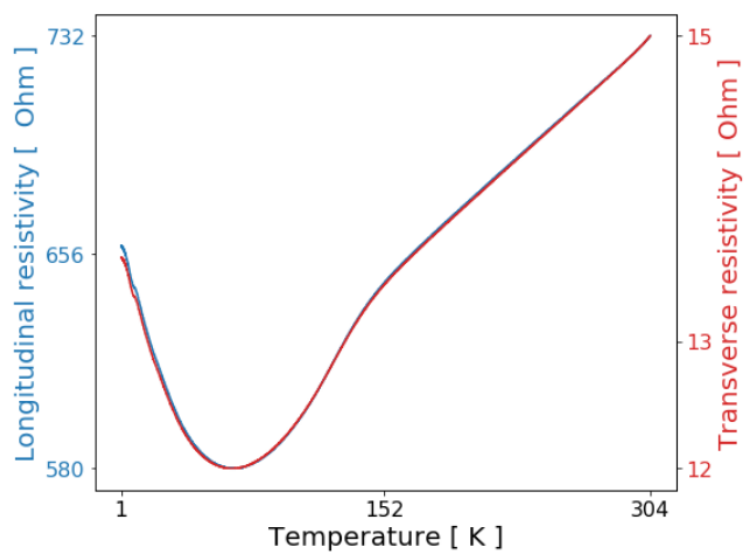


Figure 37: FM15b. Cooldown at 0 T.

5.11 APPENDIX B.11

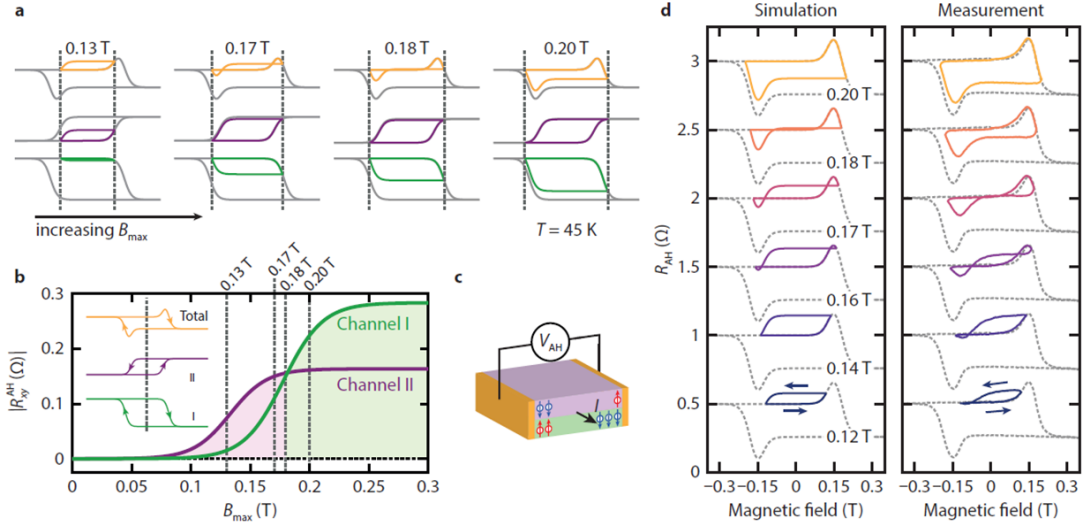


Figure 38: Taken from Ref.[44]. a) Simulations of the AHE signal for different sweep ranges. b) Magnitudes of the AHE signal for the two different channels. c) A schematic of spin accumulation on different interfaces of SrRuO_3 . d) Comparison of simulated and measured data for partial sweeps; curves are offset vertically.

Part II
BIBLIOGRAPHY

BIBLIOGRAPHY

- [1] In: <http://www.ltlab.com/optcryo105.html> ().
- [2] In: https://www.python-course.eu/graphs_python.php ().
- [3] Kundu A.K. *Magnetic Perovskites*. Springer, 2016. Chap. Introduction to Magnetic Perovskites, pp. 1–35.
- [4] N.W. Ashcroft and N.D. Mermin. *Solid State Physics*. Philadelphia: Saunders College, 1976.
- [5] Chang C.-Z. and Li M. “Quantum anomalous Hall effect in time-reversal-symmetry breaking topological insulators”. In: *Journal of Physics: Condensed Matter* 28.123002 (2016).
- [6] Schneider C.W. and Lippert T. *Laser processing of materials*. Springer, 2010. Chap. Laser ablation and thin film deposition, pp. 89–112.
- [7] Groenendijk D. “Spin-orbit coupling and geometric phases at oxide interfaces”. 2019.
- [8] Hall E.H. “On a new action of the magnet on electric currents”. In: *American Journal of Mathematics* 2 (1879), pp. 287–292.
- [9] Haldane F.D.M. “Berry Curvature on the Fermi Surface: Anomalous Hall Effect as a Topological Fermi-Liquid Property”. In: *Physical Review Letters* 93.206602 (2004).
- [10] Xiaodong Fang and Takeshi Kobayashi. “Characterization of thin film grown by laser ablation at temperatures above 400 C”. In: *Journal of Applied Physics* 90.162 (2001).
- [11] Samara G.A. “Low-temperature dielectric properties of candidate substrates for high-temperature superconductors: LaAlO₃ and ZrO₂ 9.5 mol Y₂O₃”. In: *Journal of Applied Physics* 68.4214 (1990).
- [12] Weaver H.E. “Dielectric properties of single crystals of SrTiO₃ at low temperatures”. In: *Journal of Physics and Chemistry of Solids* 11.3 (1959), pp. 274 –277.
- [13] Hwang H.Y. “Emergent phenomena at oxide interfaces”. In: *Nature Materials* 11 (2012), pp. 103–113.
- [14] Preskill J. “Magnetic Monopoles”. In: *Annual Review of Nuclear and Particle Science* 34 (1984), pp. 461–530.
- [15] Robertson J. “High dielectric constant oxides”. In: *Eur. Phys. J. Appl. Phys.* 28.3 (2004), pp. 265–291.

- [16] Chen L.-Y. "Dielectric performance of a high purity HTCC alumina at high temperatures - a comparison study with other polycrystalline alumina". In: *Additional Conferences (Device Packaging, HiTEC, HiTEN, and CICMT) 2014* (2014), pp. 271–277.
- [17] Klein L. "Comment on "Exchange bias-like phenomenon in SrRuO₃" [Appl. Phys. Lett. 88, 102502 (2006)]". In: *Applied Physics Letters* 89.036101 (2006).
- [18] Stamokostas G. L. and Fiete G. A. "Mixing of t_{2g}-eg orbitals in 4d and 5d transition metal oxides". In: *Physical Review B*. 97.085150 (2018).
- [19] Valdes L.B. "Resistivity measurements on Germanium for transistors". In: *Proc. I.R.E.* 42 (1954), pp. 420–427.
- [20] Kim M. and Min B.I. "Nature of itinerant ferromagnetism of SrRuO₃: a DFT+DMFT study". In: *Physical Review B* 91.205116 (2015).
- [21] Monteiro M. "Quantum transport at oxide interfaces". TU Delft, 2019.
- [22] Heaney M.B. *Electrical Measurement, Signal Processing and Displays*. Ed. by CRC Press. 2003. Chap. Electrical Conductivity and Resistivity.
- [23] Chang M.C. "Berry Phase in Solid State Physics". In: () .
- [24] Berry M.V. "Quantal phase factors accompanying adiabatic changes". In: *Proc. R. Soc. Lond.* 392 (1984).
- [25] Singh N. "The story of magnetism: from Heisenberg, Slater and Stoner to van Vleck, and the issues of exchange and correlation". In: *arXiv preprint 1807.11291* (2018).
- [26] Ishihara T. *Perovskite Oxide for Solid Oxide Fuel Cells*. Springer, 2009. Chap. Structure and Properties of Perovskite Oxides, pp. 1–16.
- [27] Kuech T. *Handbook of Crystal Growth: Thin Films and Epitaxy*. Elsevier, 2014.
- [28] Moriya T. and Takahashi Y. "Spin fluctuations in itinerant electron magnetism". In: *Journal de Physique Colloques* 39.C6 (1978), pp. 1466–1471.
- [29] Zwerger W. "Itinerant Ferromagnetism with Cold Atoms". In: *Science* 325.1179767 (2009).
- [30] Allen P.B. et al. "Transport properties, thermodynamic properties, and electronic structure of SrRuO₃". In: *Physical Review B* 53.8 (1996).
- [31] Asbóth J.K. et al. *A Short Course on Topological Insulators: Band Structure and Edge States in One and Two Dimensions*. Springer, 2016.
- [32] Aso R. et al. "Atomic level observation of octahedral distortions at the perovskite oxide heterointerface". In: *Scientific Reports* 3.2214 (2013).
- [33] Boschker H. et al. "Ferromagnetism and Conductivity in Atomically Thin Sr-RuO₃". In: *Phys. Rev. X*. 9.011027 (2019).

- [34] Broas M. et al. "Chemically stable atomic-layer-deposited Al₂O₃ films for processability". In: *ACS Omega* 2.7 (2017), pp. 3390–3398.
- [35] Chen Y. et al. "Weyl fermions and the anomalous Hall effect in metallic ferromagnets". In: *Physical Review B* 88.125110 (2013).
- [36] Chopdekar R.V. et al. "Disorder-induced carrier localization in ultrathin strained SrRuO₃ epitaxial films". In: *Journal of Applied Physics* 99.08F503 (2006).
- [37] Dabrowski B. et al. "Reduced ferromagnetic transition temperatures in SrRu(1-n)O₃ perovskites and Ru-site vacancies". In: *Physical Review B* 70.014423 (2004).
- [38] Dauphin A. et al. "Efficient algorithm to compute the Berry conductivity". In: *New Journal of Physics* 16 (2014).
- [39] Dodge J.S. et al. "Temperature-dependent local exchange splitting in SrRuO₃". In: *Physical Review B* 60.10 (1999).
- [40] Fang Z. et al. "The Anomalous Hall Effect and Magnetic Monopoles in Momentum Space". In: *Science* 302 (2003).
- [41] Fert A. et al. "Magnetic skyrmions: advances in physics and potential applications". In: *Nature Reviews Materials* 2.17031 (2017).
- [42] Fukui T. et al. "Chern Numbers in Discretized Brillouin Zone: Efficient Method of Computing (Spin) Hall Conductances". In: *J. Phys. Soc. Jpn.* 74 (2005), pp. 1674–1677.
- [43] Giefers H. et al. "Phonon density of states of Sn in textured SnO under high pressure: comparison of nuclear inelastic x-ray scattering spectra to a shell model". In: *Phys. Rev. B* 74.9 (2006).
- [44] Groenendijk et al. "Berry phase engineering at oxide interfaces". In: *arXiv preprint* (2018).
- [45] Groth C.W. et al. "Kwant: a software package for quantum transport". In: *New J. Phys.* 16.063065 (2014).
- [46] Grutter A.J. et al. "Evidence of high-spin Ru and universal magnetic anisotropy in SrRuO₃ thin films". In: *Physical Review B* 85.134429 (2012).
- [47] Herranz G. et al. "Enhanced electron-electron correlations in nanometric SrRuO₃ epitaxial films". In: *Physical Review B* 67.174423 (2003).
- [48] Itoh S. et al. "Weyl fermions and spin dynamics of metallic ferromagnet SrRuO₃". In: *Nature Communications* 7.11788 (2016).
- [49] Kaur P. et al. "Structural, electrical, and magnetic properties of SrRuO₃ thin films". In: *Applied Physics Letters* 104.081608 (2014).
- [50] Kim M. et al. "Intrinsic spin-orbit coupling in superconducting delta-doped Sr-TiO₃ heterostructures". In: *Physical Review B* 86.085121 (2005).

- [51] Kim S.S. et al. "Structural evolution of epitaxial SrRuO₃ thin films grown on SrTiO₃ (001)". In: *Journal of Applied Physics* 90.9 (2001).
- [52] Klein L. et al. "Anomalous Spin Scattering Effects in the Badly Metallic Itinerant Ferromagnet SrRuO₃". In: *Physical Review Letters* 77.13 (2006).
- [53] Kolesnik S. et al. "Effect of crystalline quality and substitution on magnetic anisotropy of SrRuO₃ thin films". In: *Journal of Applied Physics* 99.08F501 (2006).
- [54] Koster G. et al. "Structure, physical properties, and applications of SrRuO₃ thin films". In: *Reviews of Modern Physics* 84 (2012).
- [55] Kunkemöller S. et al. "Magnetic anisotropy of large floating-zone-grown single-crystals of SrRuO₃". In: *Crystal Research and Technology* 51.4 (2016), pp. 299–305.
- [56] Liu C.-X. et al. "The quantum anomalous Hall effect: theory and experiment". In: *Annual Review of Condensed Matter Physics* 7 (2016), pp. 301–321.
- [57] Liu J. et al. "Mechanically Tunable Magnetic Properties of Flexible SrRuO₃ Epitaxial Thin Films on Mica Substrates". In: *Advanced Electronic Materials* 4.1700522 (2018).
- [58] Lu D. et al. "Synthesis of freestanding single-crystal perovskite films and heterostructures by etching of sacrificial water-soluble layers". In: *Nature Materials* 15 (2016), pp. 1255–1261.
- [59] Mathieu R. et al. "Determination of the intrinsic anomalous Hall effect of SrRuO₃". In: *Physical Review B* 72.064426 (2005).
- [60] Matsuno J. et al. "Interface-driven topological Hall effect in SrRuO₃-SrIrO₃ bilayer". In: *Science Advances* 2.7 (2016).
- [61] Nagaosa N. et al. "Anomalous Hall effect". In: *Reviews of Modern Physics* 82 (2010), pp. 1539–1592.
- [62] Ohuchi Y. et al. "Electric-field control of anomalous and topological Hall effects in oxide bilayer thin films". In: *Nature Communications* 9.213 (2018).
- [63] Onoda S. et al. "Intrinsic Versus Extrinsic Anomalous Hall Effect in Ferromagnets". In: *Physical Review Letters* 97.126602 (2006).
- [64] Orgiani P. et al. "Strain effect on transport properties of SrRuO₃ films grown by laser MBE". In: *The European Physical Journal B* 26 (2002), pp. 23–28.
- [65] Pi L. et al. "Exchange bias-like phenomenon in SrRuO₃". In: *Applied Physics Letters* 88.102502 (2006).
- [66] Psiuk B. et al. "SrTiO₃ surface modification upon low energy Ar bombardment studied by XPS". In: *Vacuum* 131 (2016), pp. 14–21.
- [67] Qin Q. et al. "Emergence of Topological Hall Effect in a SrRuO₃ Single Layer". In: *Advanced Materials* 31.1807008 (2019).

- [68] Roy D. et al. "Field tuning of domain-wall type and chirality in SrRuO₃". In: *Physical Review B* 9.224437 (2017).
- [69] Shimizu S. et al. "Gate tuning of anomalous Hall effect in ferromagnetic metal SrRuO₃". In: *Appl. Phys. Lett.* 105.163509 (2014).
- [70] Siemons W. et al. "Dependence of the electronic structure of SrRuO₃ and its degree of correlation on cation off-stoichiometry". In: *Phys. Rev. B* 76.075126 (2007).
- [71] Singh D.J. et al. "Electronic and magnetic properties of the 4d itinerant ferromagnet SrRuO₃". In: *Journal of Applied Physics* 79.4818 (1996).
- [72] Sinwani O. et al. "Monitoring superparamagnetic Langevin behavior of individual SrRuO₃ nanostructures". In: *Physical Review B* 89.020404(R) (2014).
- [73] Sohn B. et al. "Emergence of robust 2D skyrmions in SrRuO₃ ultrathin film without the capping layer". In: *arXiv preprint 1810.01615v1* (2018).
- [74] Talbi F. et al. "Dielectric breakdown characteristics of alumina". In: *2010 10th IEEE International Conference on Solid Dielectrics* (2010).
- [75] Teodorescu C.M. et al. "Band ferromagnetism in systems of variable dimensionality". In: *Journal of Optoelectronics and Advanced Materials* 10.11 (2008).
- [76] Thouless D.J. et al. "Quantized Hall conductance in a two-dimensional periodic potential". In: *Physical Review Letters* 49.405 (1982).
- [77] Tokura Y. et al. "Emergent functions of quantum materials". In: *Nature Physics* 13 (2017), pp. 1056–1068.
- [78] Toyota D. et al. "Ferromagnetism stabilization of ultrathin SrRuO₃ films: thickness-dependent physical properties". In: *Journal of Applied Physics* 99.08N505 (2006).
- [79] Tyagi S. et al. "Strain healing of spin-orbit coupling: a cause for enhanced magnetic moment in epitaxial SrRuO₃ films". In: *arXiv:1901.00613v1* (2019).
- [80] Wang X. et al. "Fermi-surface calculation of the anomalous Hall conductivity". In: *Physical Review B* 76.195109 (2007).
- [81] Xiao D. et al. "Berry Phase effects on electronic properties". In: *Reviews of Modern Physics* 82.3 (2010), pp. 1959–2007.
- [82] Yang W.-H. et al. "LaAlO₃ single crystal substrate for epitaxial superconducting thin films". In: *Solid State Communications* 75.5 (1990), pp. 421–424.
- [83] Zhong Z. et al. "Theory of spin-orbit coupling at LaAlO₃-SrTiO₃ interfaces and SrTiO₃ surfaces". In: *Physical Review B* 87.161102(R) (2013).
- [84] Caviglia lab. "Angle-dependent field measurements, in the works." In: () .

DECLARATION

Put your declaration here.

Delft, May 19, 2019

Hélène Spring

COLOPHON

this is a brief description of publication or production notes relevant to the edition

Final Version as of May 19, 2019 (classicthesis version 1).